Natural convection heat transfer from vertical 9 x 9 rod bundles in liquid sodium

Hata, Koichi

Liu, Qiusheng

Nakajima, Takashi

(Citation)
Heat and Mass Transfer,57(5):807-828

(Issue Date)
2021-05

(Resource Type)
journal article

(Version)
Accepted Manuscript

NATURAL CONVECTION HEAT TRANSFER FROM VERTICAL 9×9 ROD BUNDLES IN LIQUID SODIUM

Koichi Hata

Graduate School of Maritime Sciences, Kobe Univ.

5-1-1, Fukae-minami, Kobe, Hyogo 658-0022, Japan

Qiusheng Liu

Graduate School of Maritime Sciences, Kobe Univ.

5-1-1, Fukae-minami, Kobe, Hyogo 658-0022, Japan

Takashi Nakajima

Institute of Advanced Energy, Kyoto Univ.

Gokasho, Uji, Kyoto 611-0011, Japan

Abstract

Natural convection heat transfer from vertical 9×9 rod bundle in liquid sodium was numerically analyzed to optimize the thermal-hydraulic design for the bundle geometry with equilateral square and triangle arrays (ESA and ETA). Unsteady laminar three-dimensional fundamental equations of natural convection heat transfer caused by step heat flux were solved numerically until the solution reached a steady state. The PHOENICS code was used to calculate the temperature dependence of the relevant thermo-physical properties. For this work, a 9×9 test rod with a diameter (D = 7.6 mm), heated length (L = 200 mm), L / d (= 26.32) was used. The surface heat flux (q) of each cylinder was equally applied. It ranged from 2×10^5 to 7×10^6 W/m^2. The modified Rayleigh number, $(Ra_{f,L})_{ij}$ and $(Ra_{f,L})_{Nx\times Ny,S/D}$, ranged from 6.430×10^5 to 4.309×10^7 at the liquid temperature of 673.15K. The value of S/D, the ratio of the diameter of the flow channel to the diameter of the rod in the bundle geometry of the vertical 9×9 rod bundle, ranged from 1.82 to 5 for the bundle geometry with ESA. The spatial distributions of the average Nusselt numbers, $(Nu_{av})_{ij}$ and $(Nu_{av,B})_{Nx\times Ny,S/D}$, were revealed for the vertical single cylinder of the rod bundle and the vertical rod bundle. To determine the effect of array

size, bundle geometry, *S/D*, $(Ra_{f,L})_{ij}$ and $(Ra_{f,L})_{Nx\times Ny,S/D}$ on heat transfer, the average Nusselt numbers, $(Nu_{av})_{ij}$ and $(Nu_{av,B})_{Nx\times Ny,S/D}$, of bundle geometries with different values of *S/D* were calculated. The general correlations for natural convection heat transfer from a vertical $N_x\times N_y$ rod bundle with the ESA and ETA including the effects of array size, $(Ra_{f,L})_{Nx\times Ny,S/D}$ and *S/D* were derived. The correlations of vertical $N_x\times N_y$ rod bundles can describe the theoretical $(Nu_{av,B})_{Nx\times Ny,S/D}$ values within -4.79% to 6.60% at S/D ranged from 1.82 to 6, and modified Rayleigh numbers ranged from 6.430×10^5 to 4.309×10^7.

Key Words: Natural Convection Heat Transfer, Liquid Sodium, Vertical 9×9 Rod Bundle, Array Size, ESA, ETA

1 Introduction

Knowledge of natural convection heat transfer from a vertical $N_x\times N_y$ rod bundle in liquid sodium is important as a database for the natural circulation and the design of a heat exchanger in a fast reactor for decay heat removal in the case of a loss of coolant accident (LOCA) and a loss of flow accident (LOFA). However, few basic experimental studies from vertical $N_x\times N_y$ rod bundles in liquid sodium have been published, and the optimal number of heating elements in the vertical rod bundle when designing a mockup experiment for a vertical rod bundle is completely unknown.

Natural convection heat transfer from a vertical and horizontal rod bundles in liquid sodium and in liquid metal has been studied both experimentally and numerically [1-13]. Recently, natural convection heat transfer from vertical 5×5 and 7×7 rod bundles in liquid sodium was numerically analyzed for two types of the bundle geometry (equilateral square and triangle arrays, ESA and ETA). In these works, 5×5 and 7×7 test rods of diameter (D = 7.6 mm), heated length (L = 200 mm), and L/d (= 26.32) were used. The surface heat flux (q) of each cylinder was given equally between 1×10^4 and 7×10^6 W/m^2 for a modified Rayleigh number, $(Ra_{f,L})_{ij}$ and $(Ra_{f,L})_{Nx\times Ny,S/D}$, ranging from 3.08×10^4 to 4.28×10^7 at liquid temperature (T_L = 673.15 K). The *S/D* value, which is the ratio of the diameter of the flow channel to the rod diameter of the bundle geometry, for vertical 5×5 and 7×7 rod bundles, was ranged from 1.8 to 6 on each bundle geometry. The spatial distribution of the average Nusselt number of the vertical single cylinder, $(Nu_{av})_{ij}$, of the rod bundle and the average Nusselt number, $(Nu_{av,B})_{Nx\times Ny,S/D}$, of the vertical rod bundle was revealed. The effects of array size, bundle geometry, *S/D*, $(Ra_{f,L})_{ij}$ and $(Ra_{f,L})_{Nx\times Ny,S/D}$ on heat transfer were investigated by calculating the average Nusselt number, $(Nu_{av})_{ij}$ and $(Nu_{av,B})_{Nx\times Ny,S/D}$, for two types of bundle geometry with different values of *S/D*. Under the condition of *S/D* = constant, bundle geometry with higher $(Nu_{av,B})_{Nx\times Ny,S/D}$ value was investigated. The general correlations for natural convection heat transfer from vertical 5×5 and 7×7 rod bundles with the ESA and ETA including the effects of array size, $(Ra_{f,L})_{Nx\times Ny,S/D}$ and *S/D* were developed. The correlation of vertical 5×5 and 7×7 rod bundles can

explain the theoretical value of $(Nu_{av,B})_{Nx\times Ny,S/D}$ for each bundle geometry within a difference of -12.64 to 10.6% over a wide analysis range of S/D (=1.8 to 6) and modified Rayleigh number ($(Ra_{f,L})_{Nx\times Ny,S/D}$=3.08×10^4 to 4.28×10^7) [14-18].

Table 1 shows the number of heating elements used in the experimental and numerical studies of natural convection heat transfer from rod bundle in liquid metals that have been reported so far as mentioned above. The number of heating elements is wide ranging from 1 to 61 pins in the experimental studies and from 1 to 271 pins in the numerical studies. The heat transfer from the rod bundle is considered to be lower than that from a single test cylinder in the liquid metals due to the effect of S/D for the bundle geometry; however, few basic experimental studies from vertical $N_x\times N_y$ rod bundles in liquid metals have been published. It is important to clarify the minimum number of heating elements that gives the optimum value for natural convection heat transfer from the rod bundle in the numerical studies.

The purpose of this study is as follows: (1) to analyze theoretically the natural convection heat transfer from the vertical 9×9 rod bundle with a geometry of ESA in liquid sodium, (2) to obtain the numerical solutions of the average Nusselt number of a vertical single cylinder of a rod bundle, $(Nu_{av})_{ij}$, and the average Nusselt number of a vertical 9×9 rod bundle, $(Nu_{av,B})_{9\times 9,S/D}$, in wide ranges of $(Ra_{f,L})_{ij}$, $(Ra_{f,L})_{9\times 9,S/D}$ and S/D, (3) to clarify the effect of array size, $(Ra_{f,L})_{ij}$, $(Ra_{f,L})_{9\times 9,S/D}$ and S/D on heat transfer, and (4) to derive general correlations for natural convection heat transfer from a vertical $N_x\times N_y$ rod bundle with ESA and ETA, (5) to clarify the optimum number of heating elements in the vertical rod bundle when designing a Mock-up Experiment to reliably and accurately measure the typical Nusselt number, $(Nu_{av,B})_{Nx\times Ny,S/D}$, from a vertical $N_x\times N_y$ rod bundle with ESA and ETA.

2 Apparatus and method

Figure 1 schematically shows a half model of the test vessel. It is a cubic container 288 mm wide, 320 mm long and 470 mm high and contains about 43.32 liters of liquid sodium. A 9×9 rod bundle with 81 single test cylinders with a diameter D = 7.6 mm was mounted perpendicular to the central axis of the vessel. As shown in Fig. 2, natural convection heat transfer from a vertical 9×9 rod bundle is numerically analyzed for bundle geometry with ESA. The 9×9 test cylinders with ESA are mounted vertically at even intervals on circumference of diameter S mm with a central axis of the vessel. The diameter of the flow channel in the bundle geometry is defined as S mm by the chimney effect (buoyancy driven flow).

3 Theoretical solution of laminar natural convection equations

3.1 Fundamental equations

Considering the half symmetric model of the calculation problem with ESA shown in Fig. 2, the unsteady laminar three-dimensional basic equations in the boundary fitted coordinates of ESA in Figs. 3 (a) and (b) are as follows:

(Continuity Equation)

$$\frac{\partial \rho}{\partial t}+\frac{\partial}{\partial x}(\rho u)+\frac{\partial}{\partial y}(\rho v)+\frac{\partial}{\partial z}(\rho w)=0 \tag{1}$$

(Momentum Equation)

$$\frac{\partial}{\partial t}(\rho u)+\frac{\partial}{\partial x}(\rho uu)+\frac{\partial}{\partial y}(\rho vu)+\frac{\partial}{\partial z}(\rho wu)=-\frac{\partial P}{\partial x}+\left(\frac{\partial}{\partial x}\tau_{xx}+\frac{\partial}{\partial y}\tau_{yx}+\frac{\partial}{\partial z}\tau_{zx}\right) \tag{2}$$

$$\frac{\partial}{\partial t}(\rho v)+\frac{\partial}{\partial x}(\rho uv)+\frac{\partial}{\partial y}(\rho vv)+\frac{\partial}{\partial z}(\rho wv)=-\frac{\partial P}{\partial y}+\left(\frac{\partial}{\partial x}\tau_{xy}+\frac{\partial}{\partial y}\tau_{yy}+\frac{\partial}{\partial z}\tau_{zy}\right) \tag{3}$$

$$\frac{\partial}{\partial t}(\rho w)+\frac{\partial}{\partial x}(\rho uw)+\frac{\partial}{\partial y}(\rho vw)+\frac{\partial}{\partial z}(\rho ww)=-\frac{\partial P}{\partial z}+\left(\frac{\partial}{\partial x}\tau_{xz}+\frac{\partial}{\partial y}\tau_{yz}+\frac{\partial}{\partial z}\tau_{zz}\right)+\rho g_z \tag{4}$$

(Energy Equation)

$$\frac{\partial}{\partial t}(\rho c_p T)+\frac{\partial}{\partial x}(\rho c_p uT)+\frac{\partial}{\partial y}(\rho c_p vT)+\frac{\partial}{\partial z}(\rho c_p wT)=\frac{\partial}{\partial x}\left\{\frac{\lambda}{c_p}\left(c_p\frac{\partial T}{\partial x}\right)\right\}+\frac{\partial}{\partial y}\left\{\frac{\lambda}{c_p}\left(c_p\frac{\partial T}{\partial y}\right)\right\}+\frac{\partial}{\partial z}\left\{\frac{\lambda}{c_p}\left(c_p\frac{\partial T}{\partial z}\right)\right\} \tag{5}$$

where

$$\tau_{xx}=2\rho\nu\frac{\partial u}{\partial x},\quad \tau_{yy}=2\rho\nu\frac{\partial v}{\partial y},\quad \tau_{zz}=2\rho\nu\frac{\partial w}{\partial z} \tag{6}$$

$$\tau_{xy}=\tau_{yx}=\rho\nu\left(\frac{\partial u}{\partial y}+\frac{\partial v}{\partial x}\right),\ \tau_{yz}=\tau_{zy}=\rho\nu\left(\frac{\partial v}{\partial z}+\frac{\partial w}{\partial y}\right),\quad \tau_{zx}=\tau_{xz}=\rho\nu\left(\frac{\partial w}{\partial x}+\frac{\partial u}{\partial z}\right) \tag{7}$$

u, v, and w are the x, y, and z components of the velocity vector, respectively.

3.2 Boundary conditions

The calculation domain for 1/2 symmetry model of a cubic vessel with a width of 288 mm, a length of 320 mm and a height of 470 mm was divided into 100, 257, and 37 grid points for the x, y, and z components. The first control volume width for r-component, Δr (=Δx and Δy), on the heated section was determined as 0.4 mm as shown in Figs. 3 (a) and (b) [14-18]. The time step, Δt, was set to 3 ms. The basic equations are analyzed numerically with the following boundary conditions:

On the surfaces of cylinders: constant heat flux and nonslip condition.

At the outer boundary of test vessel:

$$T = T_0, \quad \frac{\partial u}{\partial x} = 0 \quad \text{and} \quad T = T_0, \quad \frac{\partial v}{\partial y} = 0 \qquad \text{for inflow} \qquad (8)$$

$$\frac{\partial T}{\partial x} \simeq 0, \quad \frac{\partial u}{\partial x} = 0 \quad \text{and} \quad \frac{\partial T}{\partial y} \simeq 0, \quad \frac{\partial v}{\partial y} = 0 \qquad \text{for outflow} \qquad (9)$$

At the lower and upper boundaries:

$$T = T_0, \quad \frac{\partial w}{\partial z} = 0 \qquad \text{for inflow} \qquad (10)$$

$$\frac{\partial T}{\partial z} \simeq 0, \quad \frac{\partial w}{\partial z} = 0 \qquad \text{for outflow} \qquad (11)$$

where T_0 is a bulk liquid temperature.

3.3 Method of solution

These basic equations were discretized using a hybrid scheme [19], and the control volume discretization equations were obtained. The thermophysical properties of each control volume, such as specific heat at constant pressure (c_p), thermal conductivity (λ), viscosity (μ), and density (ρ), are given as values at each control volume temperature. The calculation procedure for the flow field is the SIMPLE algorithm, which represents a Semi-Implicit Method for Pressure-Linked Equations.

The initial conditions at start time t = 0 s are 0.0005 m/s for velocities u, v and w, respectively, and 673.15 K for bulk liquid temperature T_L. The surface heat fluxes, q, for each cylinder were equally given in the range of 2×10^5, 7×10^5, 1×10^6, 2×10^6 and 7×10^6 W/m^2 as an initial condition, and numerical calculations continued until a steady state was obtained. The surface temperature of the cylinder was analyzed by solving the heat conduction equation in liquid sodium, assuming that the calculated temperature, *TEM*, of the first control volume of the heated surface was located at the center of the control volume, as follows [14-18]:

$$T_s = \frac{q}{\lambda_l}\frac{(\Delta r)_{out}}{2} + TEM \qquad (12)$$

where, $(\Delta r)_{out}$ is the first control volume width for the r-component. In Fig. 4, the test cylinder surface is located at r=0 mm and the conductive sub-layer [14-18, 20, 21] exists on the test cylinder surface. The liquid temperatures in the conductive sub-layer on the test cylinder surface will become linearly lower with an increase in the radius by the heat conduction from the surface temperature on the test cylinder, $T_f=T_s-(q/\lambda_l)[(\Delta r)_{out}/2)]$. And let those, T_f, equal to the analyzed liquid temperature of the first control volume on the test cylinder surface, *TEM*, as given in Eq. (12). Half of the first control volume width of the r component, $(\Delta r)_{out}/2$, is the thickness of the conductive sublayer, δ_{CSL}, of local heat transfer on a vertical cylinder under a two-phase model classified into the laminar sublayer and the transition region of buoyancy-driven flow. Average heat transfer coefficient on each cylinder surface was obtained by averaging

the calculated 36 (θ direction) × 20 (z direction) local surface temperatures at every 10 degrees and mm, $(T_{s,av})_{i,j}=(1/N_z)\int_1^{Nz}(1/N_\theta)\int_1^{N\theta}\{T_s(\theta, z)_{i,j}\, d\theta\, dz$, in the heated length, L, of 200 mm. All the calculations were carried out by using the commercial CFD code PHOENICS [22].

4 Results and discussion

In this section, previously obtained correlations are firstly explained for natural convection heat transfer from a vertical single cylinder and vertical 5×5 and 7×7 rod bundles with ESA and ETA. The general correlations for vertical $N_x \times N_y$ rod bundles with ESA and ETA are derived by the use of the following correlation for a vertical single cylinder.

4.1 Correlation for a vertical single cylinder (N=1) previously obtained [14]

4.1.1 Local Nusselt number

The local Nusselt number, Nu_z, for the experimental data and the numerical solutions from liquid sodium and the numerical solutions from air are approximately expressed by the following correlation [14, 23-25].

$$Nu_z = \left[1+\frac{C}{\left(Ra_z^*\right)^{0.2}}\left(\frac{z}{D}\right)^{0.86}\right] Ra_f^{\,0.2} \qquad \text{for } 2.1\times10 \le Ra_f \le 4.3\times10^6 \tag{13}$$

where $$C = 0.85\left(\frac{Pr}{4+9Pr^{1/2}+10Pr}\right)^{-0.2} \tag{14}$$

$$Ra_z^* = Gr_z^* Pr \tag{15}$$

$$Gr_z^* = \frac{g\beta\, qz^4}{\lambda\nu^2} \tag{16}$$

$$Ra_f = \frac{Gr_z^* Pr^2}{4+9Pr^{1/2}+10Pr} \tag{17}$$

For liquid sodium with a liquid temperature of 673 to 873 K, C is constant in the range of 3.258 to 3.375 and is approximately equal to 3.36. The Nu_z curve derived from the correlation Eq. (13) is consistent with the experimental data and numerical solution for a vertical single cylinder within a 20% difference.

Experimental data for the local surface temperature rise, $(T_s)_z$-T_L, of a vertical single test cylinder are shown in Fig. 5 against the vertical distance from the leading edge of the heated section, z, with black symbols for the heat fluxes, q, of 2×10^5, 7×10^5, 1×10^6 and 2×10^6 W/m^2 at a liquid temperature of about 773.15 K. Numerical solutions numerically analyzed natural convection heat transfer at the liquid temperatures of 773.15 K are also included as a black solid line with red circle in the figure. At a constant heat flux q, the rate of increase of the $(T_s)_z$-T_L is steep near the leading edge of the heated section, and becomes gradually slower at z greater than 30 mm. The value obtained from Eq. (13) is shown in

the figure as a red dashed line for comparison. These temperature distributions are almost in good agreement with those for the experimental data and the numerical solutions on a vertical single cylinder within -14.91 to 18.25 % differences and -8.14 to -2.52 % ones [14, 15].

4.1.2 Average Nusselt number

The average Nusselt number, Nu_{av}, is expressed as follows from Eq. (13).

$$Nu_{av} = \left[\frac{1}{0.8} + \frac{C}{0.86\left(Ra_L^*\right)^{0.2}} \left(\frac{L}{D} \right)^{0.86} \right] Ra_{f,L}^{0.2} \qquad \text{for } 3.06\times10^4 \le Ra_{f,L} \le 3.14\times10^7 \tag{18}$$

where $Ra_L^* = Gr_L^* Pr$ (19)

$$Gr_L^* = \frac{g\beta\, qL^4}{\lambda \nu^2} \tag{20}$$

$$Ra_{f,L} = \frac{Gr_L^* Pr^2}{4 + 9Pr^{1/2} + 10Pr} \tag{21}$$

The average Nusselt numbers, Nu_{av}, derived from the correlation, Eq. (18), for a vertical single test cylinder with a diameter of 7.6 mm and a heated length of 200 mm are 41.502 and 45.511 for the heat fluxes of 1×10^6 and 2×10^6 W/m^2 at the liquid temperature of 673.15 K, and they are 42.386 and 46.576 for the heat fluxes of 1×10^6 and 2×10^6 W/m^2 at the liquid temperature of 773.15 K.

4.1.3 Thickness of average conductive sub-layer on laminar natural convection heat transfer, $\delta_{CSL,av}$

A typical example of a laminar natural convection heat transfer curve with a vertical cylinder diameter of 7.62 mm, a heated length of 186 mm, and a heated length-to-cylinder diameter ratio of 24.41 at a liquid temperature of about 773.15 K is re-plotted in Fig. 6 versus the temperature difference, ΔT_L (=$T_{s,av}$-T_L) [14]. The numerical solution of the relationship between the heat flux, q, and the temperature difference between the average surface temperature and the liquid bulk average temperature, ΔT_L, is shown by the solid green circle. As shown in Fig. 6, the numerical solution of the theoretical equations for laminar natural convection agrees well with the experimental data and the value derived from Eq. (18) within -15% errors. The average conductive sublayer thickness, $\delta_{CSL,av}$, for laminar natural convection heat transfer on a vertical cylinder with D = 7.62 mm and L = 186 mm in Fig. 6 is 200 μm. The thickness of the average conduction sub-layer does not depend on the heat flux and the heater surface temperature, and is almost constant at 200 μm in the wide ΔT_L region. The Prandtl numbers of the heated surface of the vertical cylinder on laminar natural convection, $(Pr)_{TEM,av}$, are evaluated at the average calculated temperature of the first control volume on the heated

surface, TEM_{av}, and are indicated by a blue solid line in Fig. 6. As shown in Fig. 7, the Prandtl numbers of sodium are given by the following equation with respect to the sodium temperature.

$$Pr=a_6\times T^6+a_5\times T^5+a_4\times T^4+a_3\times T^3+a_2\times T^2+a_1\times T+a_0 \quad (22)$$

where a_0=1.269875*E*-01, a_1=-8.057894*E*-04, a_2=2.248745*E*-06, a_3=-3.338381*E*-09, a_4=2.748397*E*-12, a_5=-1.184295*E*-15 and a_6=2.083333*E*-19. The Prandtl number is 0.0046294 at ΔT_L=18.726 K in Fig. 6. It decreases gradually with an increase in ΔT_L and becomes the minimum value 0.0041735 at ΔT_L =145.023 K. The Prandtl number of sodium is much smaller than 1. The thicknesses of average conductive sub-layer, $\delta_{CSL,av}$, are also shown in Fig. 6. The thickness of the average conduction sub-layer is a constant value of 200 μm in the wide ΔT_L region. Results of scale analysis in laminar thermal boundary layers give the order of magnitude of the main values shown in following equations [20, 21]:

$$\delta_{VSL,av}/\delta_{CSL,av}=Pr^{1/2} \quad \text{for } Pr<<1 \quad (23)$$

$$\delta_{VSL,av}/\delta_{CSL,av}=1 \quad \text{for } Pr=1 \quad (24)$$

$$\delta_{VSL,av}/\delta_{CSL,av}=Pr^{1/3} \quad \text{for } Pr>1 \quad (25)$$

The thicknesses of the average viscous sub-layer, $\delta_{VSL,av}$, for the laminar natural convection heat transfer on the vertical cylinder of D=7.62 mm and L=186 mm are estimated from the thicknesses of the average conductive sub-layer, and Prandtl numbers are evaluated at the average calculated temperature of the first control volume on the heated surface. These values are shown with a red broken line in Fig. 6, and they are also listed in Table 2. The thickness of the average viscous sub-layer, $\delta_{VSL,av}$, is 13.608 μm at ΔT_L=18.726 K. It decreases gradually as ΔT_L increases, and becomes the minimum value of 12.9206 μm at ΔT_L =145.023K. The decreasing trend is similar to Prandtl number, $(Pr)_{TEM,av}$.

The thickness of the local conductive sub-layer, δ_{CSL}, for the laminar natural convection heat transfer on the vertical cylinder of D=7.62 mm and L=186 mm is also constant at 200 μm in the wide range of heater surface temperature, T_s. The thickness of the local conductive sub-layer, δ_{CSL}, does not also depend on the heat flux and the heater surface temperature, it is a constant value of 200 μm in the wide ΔT_L region. Therefore, the thickness of the average conductive sub-layer, $\delta_{CSL,av}$, is exactly the same value as the thickness of the local conductive sub-layer, δ_{CSL}. The thickness of the local viscous sub-layer, δ_{VSL}, for the laminar natural convection heat transfer are estimated from the thickness of the local conductive sub-layer, δ_{CSL}, and Prandtl numbers evaluated at the calculated temperature of the first control volume on the heated surface, $(Pr)_{TEM}$. The detailed description about thicknesses of local conductive and viscous sub-layers, δ_{CSL} and δ_{VSL}, on the laminar natural convection heat transfer is made in Appendix A.1.

4.2 Previously obtained correlations for natural convection heat transfer from vertical 7×7 rod bundles at various *S/D* [16, 18]

General correlations of natural convection heat transfer from vertical 7×7 rod bundles in ESA and ETA in liquid sodium are given in the correlations for vertical 5×5 rod bundles with the ESA and ETA based on the numerical solutions as follows [16, 18]:

$$\left(Nu_{av,B}\right)_{N_x\times N_y,S/D} = C_1\times\left(Ra_{f,L}\right)^{n}_{N_x\times N_y,S/D}\times\left[\frac{1}{0.8}+\frac{C}{0.86\left(Ra_L^*\right)^{0.2}}\left(\frac{L}{D}\right)^{0.86}\right]\left(Ra_{f,L}\right)^{0.2}_{N_x\times N_y,S/D} \text{ for } 3.08\times10^4\le Ra_{f,L}\le 4.24\times10^7 \quad (26)$$

where

In the case of ESA:
$$C_1 = 0.00394\times\left(\frac{S}{D}\right)^{2.47} \quad (27)$$

$$n = 0.267-0.0341\times\left(\frac{S}{D}\right) \quad (28)$$

In the case of ETA:
$$C_1 = 0.00550\times\left(\frac{S}{D}\right)^{2.52} \quad (29)$$

$$n = 0.263-0.0390\times\left(\frac{S}{D}\right) \quad (30)$$

The numerical solutions for $(Nu_{av,B})_{Nx\times Ny,S/D}$ with ESA are in good agreement with the values given by the authors' correlations, Eqs. (26), (27) and (28), within -9.49 to 4.4 % differences under the wide range of $(Ra_{f,B})_{Nx\times Ny,S/D}$ and *S/D* as shown in Fig. 8.

The effect of *S / D* on the average Nusselt number, $(Nu_{av,B})_{Nx\times Ny,S/D}$, from a vertical 7×7 rod bundle with the ESA and ETA is generally estimated based on the numerical solutions for the *S/D* ranging from 1.8 to 6 at the constant heat flux, *q*, of 1×10^6 W/m^2 ($(Ra_{f,L})_{Nx\times Ny,S/D}= 3.54\times10^6$). The values of $(Nu_{av,B})_{Nx\times Ny,S/D}$ for vertical $N_x\times N_y$ rod bundles with ESA and ETA can be expressed by the following empirical correlations [16, 18]:

In the case of ESA: $\left(Nu_{av,B}\right)_{N_x\times N_y,S/D} = 2.21+24.5\times ln\left(\frac{S}{D}\right)$ for $1.8\le S/D\le 4.47$ (31)

$\left(Nu_{av,B}\right)_{N_x\times N_y,S/D} = Nu_{av} = 38.88$ for $4.47\le S/D\le 6$ (32)

In the case of ETA: $\left(Nu_{av,B}\right)_{N_x\times N_y,S/D} = 5.89+24.5\times ln\left(\frac{S}{D}\right)$ for $1.8\le S/D\le 3.84$ (33)

$\left(Nu_{av,B}\right)_{N_x\times N_y,S/D} = Nu_{av} = 38.88$ for $3.84\le S/D\le 6$ (34)

The numerical solutions for $(Nu_{av,B})_{Nx\times Ny,S/D}$ with ESA are in good agreement with the values given by the authors' correlations, Eqs. (31) and (32), within -4.65 to 10.60 % differences under the wide range of *S/D* as shown in Fig. 9.

4.3 Calculated results for vertical 9×9 rod bundle with ESA

Natural convection heat transfer from a vertical 9×9 rod bundle was numerically analyzed for the bundle geometry of an ESA as shown in Figs. 1 to 3. The *S/D* of the rod bundle on the bundle geometry, which is the ratio of the diameter of the flow channel to the rod diameter of the bundle geometry, ranged from 1.82 to 5 at ESA. The surface heat fluxes of each cylinder were given by 2×10^5, 7×10^5, 1×10^6, 2×10^6 and 7×10^6 W/m^2. Table 3 shows the parameters used for the calculation.

4.3.1 Relationship between $(Nu_{av})_{ij}$ and, N_x and N_y

Numerical results for the average Nusselt number of each vertical single cylinder, $(Nu_{av})_{ij}$ $(=qL/[2\lambda_l\{(T_{s,av})_{ij}-T_L)\}])$, on a rod bundle of a 9×9 array of ESA with *S/D* = 2 for $(Ra_{f,L})_{ij}=3.678\times10^6$ ($q=1\times10^6$ W/m^2) are shown in Figs. 10 and 11 as typical examples. The average surface temperature, $(T_{s,av})_{ij}$, average Nusselt number, $(Nu_{av})_{ij}$, and modified Rayleigh number, $(Ra_{f,L})_{ij}$, of a vertical single cylinder of an $N_x\times N_y$ array rod bundle were obtained as follows:

$$(T_{s,av})_{ij}=\frac{1}{N_z}\int_1^{N_z}\frac{1}{N_\theta}\int_1^{N\theta}\{T_s(\theta,z)\}_{ij}\,d\theta dz \tag{35}$$

$$(Nu_{av})_{ij}=\frac{qL}{2\lambda_l\{(T_{s,av})_{ij}-T_L\}} \tag{36}$$

$$(Ra_{f,L})_{ij}=\frac{(Gr_L^*)_{ij}(Pr)_{ij}^2}{4+9(Pr)_{ij}^{1/2}+10(Pr)_{ij}} \tag{37}$$

These are displayed as $(Nu_{av})_{ij}$ versus N_x and N_y graphs with N_y and N_x as parameters, respectively, where N_i and N_x are column numbers, N_j and N_y are row numbers (N_i = 1 and 9 are edge columns, N_i = 5 is center column, N_j = 1 and 9 are edge rows, and N_j = 5 is center row). $(Nu_{av})_{ij}$ values are almost symmetric on the graph in Fig. 10, because the computation domain is half of the symmetric model for the N_y axis at N_i = 5. The value of $(Nu_{av})_{ij}$ in each column of N_j = 1 and 9 (edge row) is higher than the values in other rows. The 4 values of $(Nu_{av})_{ij}$ at N_i=1 and 9 for N_j=1 and 9 (), $(Nu_{av})_{11}$, $(Nu_{av})_{19}$, $(Nu_{av})_{91}$, and $(Nu_{av})_{99}$, are near maximum. The value of $(Nu_{av})_{ij}$ in each column decreases as the row number increases and decreases from the edge row. The 49 values of $(Nu_{av})_{ij}$ at N_i=2, 3, 4, 5, 6, 7 and 8 for N_j=2, 3, 4, 5, 6, 7 and 8 () are almost minimal. The values of $(Nu_{av})_{ij}$ at N_j=2, 3, 4, 5, 6, 7 and 8 () for N_i=1 and 9 (edge column) and those at N_i=2, 3, 4, 5, 6, 7 and 8 () for N_j=1 and 9 (edge row) are higher than those for other columns and rows on the same row and column numbers, respectively. The average value of $(Nu_{av})_{ij}$ at N_j=2, 3, 4, 5, 6, 7 and 8 () for N_i=1 and 9 (edge column) are 7.35 % higher than those at N_i=2, 3, 4, 5, 6, 7 and 8 for N_j=1 and 9 (edge row). The values of 14 for $(Nu_{av})_{ij}$ at N_i = 2, 3, 4, 5, 6, 7 and 8 () for N_j = 1 and 9 (edge rows) are approximately centered. The values of 81 for $(Nu_{av})_{ij}$ at N_j = 1 to 9 at N_i = 1 to 9 are significantly 14.53 to 65.12% lower than the value for the

vertical single cylinder.

4.3.2 Relationship between $(Nu_{av})_{ij}$ and, $(N_i\text{-}1)/(N_x\text{-}1)$ and $(N_j\text{-}1)/(N_y\text{-}1)$

Numerical results of the average Nusselt number of each vertical single cylinder, $(Nu_{av})_{ij}$, on a rod bundle of 9×9 array of ESA with S/D = 2 for $(Ra_{f,L})_{ij}$ =3.678×10^6 were also shown in Figs. 12 and 13 as pink symbols. These are shown as graphs of $(Nu_{av})_{ij}$ versus dimensionless column numbers, $(N_i\text{-}1)/(N_x\text{-}1)$, and dimensionless row numbers, $(N_j\text{-}1)/(N_y\text{-}1)$, with $(N_j\text{-}1)/(N_y\text{-}1)$ and $(N_i\text{-}1)/(N_x\text{-}1)$ as parameters, respectively. It should be mentioned that in the case of $(N_i\text{-}1)/(N_x\text{-}1)$=0 and 1, it means edge column, in the case of $(N_i\text{-}1)/(N_x\text{-}1)$=0.5, it means center column, in the case of $(N_j\text{-}1)/(N_y\text{-}1)$=0 or 1, it means edge row, and in the case of $(N_j\text{-}1)/(N_y\text{-}1)$=0.5, it means center row. Numerical results of the average Nusselt number for each vertical single cylinder, $(Nu_{av})_{ij}$, on rod bundles of 5×5 and 7×7 arrays of an ESA with S/D=2 for $(R_{f,L})_{ij}$ =3.54×10^6 (q=1×10^6 W/m^2) were also plotted on $(Nu_{av})_{ij}$ versus $(N_i\text{-}1)/(N_x\text{-}1)$ and $(N_j\text{-}1)/(N_y\text{-}1)$ graphs in the figures as green and sky-blue symbols for comparison, respectively [16, 18]. As shown in the figures, the four values of $(Nu_{av})_{ij}$ (=33.228) at $(N_i\text{-}1)/(N_x\text{-}1)$=0 and 1 for $(N_j\text{-}1)/(N_y\text{-}1)$=0 and 1 on a 9×9 array (◯), $(Nu_{av})_{11}$, $(Nu_{av})_{19}$, $(Nu_{av})_{91}$, and $(Nu_{av})_{99}$, are 15.59 and 9.98 % higher than those ($(Nu_{av})_{ij}$=28.747) on 5×5 array, $(Nu_{av})_{11}$, $(Nu_{av})_{15}$, $(Nu_{av})_{51}$, and $(Nu_{av})_{55}$ and those ($(Nu_{av})_{ij}$=30.212) on 7×7 array, $(Nu_{av})_{11}$, $(Nu_{av})_{17}$, $(Nu_{av})_{71}$, and $(Nu_{av})_{77}$, respectively. The 14 values of $(Nu_{av})_{ij}$ (=27.419) at $(N_j\text{-}1)/(N_y\text{-}1)$=0.125, 0.25, 0.375, 0.5, 0.625, 0.75 and 0.875 for $(N_i\text{-}1)/(N_x\text{-}1)$=0 and 1 (edge column) on a 9×9 array (◯) are 30.57% higher than the six values of $(Nu_{av})_{ij}$ (=20.999) at $(N_j\text{-}1)/(N_y\text{-}1)$=0.25, 0.5 and 0.75 for $(N_i\text{-}1)/(N_x\text{-}1)$=0 and 1 (edge column) on a 5×5 array, and 7.75 % higher than the ten values of $(Nu_{av})_{ij}$ (=25.447) at $(N_j\text{-}1)/(N_y\text{-}1)$=0.167, 0.333, 0.5, 0.667 and 0.833 for $(N_i\text{-}1)/(N_x\text{-}1)$=0 and 1 (edge column) on a 7×7 array. The 14 values of $(Nu_{av})_{ij}$ (=25.435) at $(N_i\text{-}1)/(N_x\text{-}1)$=0.125, 0.25, 0.375, 0.5, 0.625, 0.75 and 0.875 for $(N_j\text{-}1)/(N_y\text{-}1)$=0 and 1 (edge row) on a 9×9 array (◯) are 24.33 % higher than the six values of $(Nu_{av})_{ij}$ (=20.458) at $(N_i\text{-}1)/(N_x\text{-}1)$=0.25, 0.5 and 0.75 for $(N_j\text{-}1)/(N_y\text{-}1)$=0 and 1 (edge row) on a 5×5 array, and 14.64 % higher than the ten values of $(Nu_{av})_{ij}$ (=22.186) at $(N_i\text{-}1)/(N_x\text{-}1)$=0.167, 0.333, 0.5, 0.667 and 0.833 for $(N_j\text{-}1)/(N_y\text{-}1)$=0 and 1 (edge row) on a 7×7 array. The values of $(Nu_{av})_{ij}$ at $(N_i\text{-}1)/(N_x\text{-}1)$=0 and 1 (edge column) and $(N_j\text{-}1)/(N_y\text{-}1)$=0 and 1 (edge row) become higher with an increase in an array size, since the buoyancy driven flow increases. However, the 49 values of $(Nu_{av})_{ij}$ (=13.560) at $(N_i\text{-}1)/(N_x\text{-}1)$=0.125, 0.25, 0.375, 0.5, 0.625, 0.75 and 0.875 for $(N_j\text{-}1)/(N_y\text{-}1)$= 0.125, 0.25, 0.375, 0.5, 0.625, 0.75 and 0.875 on a 9×9 array (◯) are also the same with the nine values of $(Nu_{av})_{ij}$ (=12.934) at $(N_i\text{-}1)/(N_x\text{-}1)$=0.25, 0.5 and 0.75 for $(N_j\text{-}1)/(N_y\text{-}1)$=0.25, 0.5 and 0.75 on a 5×5 array and the 25 values of $(Nu_{av})_{ij}$ (=13.074) at $(N_i\text{-}1)/(N_x\text{-}1)$=0.167, 0.333, 0.5, 0.667 and 0.833 for $(N_j\text{-}1)/(N_y\text{-}1)$=0.167, 0.333, 0.5, 0.667 and 0.833 on a 7×7 array. Numerical results of the average Nusselt number for each vertical single cylinder, $(Nu_{av})_{ij}$, from a vertical 5×5 rod bundle seem to derive the general numerical solutions from a vertical N_x×N_y rod bundle, although the values of $(Nu_{av})_{ij}$ at $(N_i\text{-}1)/(N_x\text{-}1)$=0 and 1 (edge

column) and $(N_j\text{-}1)/(N_y\text{-}1)$=0 and 1 (edge row) become higher with an increase in array size.

4.3.3 Contours of liquid temperature and velocity vector

Liquid temperature contours in the *x*-*y* plane at *z* = 25, 95, and 195 mm (*iz* = 11, 18 and 28) for a vertical 9×9 rod bundle of an ESA with *S/D* = 2 at $(Ra_{f,L})_{9\times9,S/D=2}=3.678\times10^6$ ($q=1\times10^6$ W/m^2) were plotted in Fig. 14. It is recognized that the liquid temperatures of the flow channels for bundle geometry became higher at circumference of the center cylinder and those became also higher with an increase in the vertical distance from the leading edge of the heated section, *z*, as previously described in [15, 16, 18]. Liquid temperature contours at the *x*-*z* plane on *iy*=127 and at the *y*-*z* plane on *ix*=1 for vertical 9×9 rod bundle of ESA with *S/D* = 2 for $(Ra_{f,L})_{9\times9,S/D=2}=3.678\times10^6$ were plotted at the *x*-*z* plane on the mesh number *iy*=127 and at the *y*-*z* plane on the mesh number *ix*=1 in Fig. 15. It has been recognized that the liquid temperatures in the edge columns and rows are lower at the leading edge of the heated section, and the liquid temperatures in the center column and row are higher and increase with increasing vertical distance from the leading edge of the heated section, *z*, as previously described in [15, 16, 18]. Distribution of velocity vector on vertical 9×9 rod bundle of ESA at *S/D* = 2 for $(Ra_{f,L})_{9\times9,S/D=2}=3.678\times10^6$ were plotted at the *x*-*y* plane on the mesh number *iz*=1, 11, 18, 28 and 37 in Fig. 16. It is also recognized that a flow of liquid sodium turns to the center column and row, and rises along the center rod [15, 16, 18].

5 Correlations for vertical 9×9 rod bundle

The numerical solutions were numerically analyzed for natural convection heat transfer from vertical 9×9 rod bundle in liquid sodium with the ESA bundle geometry. In this section the correlations for the vertical $N_x\times N_y$ rod bundle including the effects of array size, *S/D* and $(Ra_{f,L})_{Nx\times Ny,S/D}$ are derived based on a numerical solution.

5.1 Calculation results of average Nusselt number, $(Nu_{av,B})_{Nx\times Ny,S/D=2}$, of vertical 9×9 rod bundle with *S/D* = 2

Numerical solutions of average heat transfer coefficients from vertical 9×9 rod bundle of ESA with *S*/*D*=2 are plotted on $(Nu_{av,B})_{Nx\times Ny,S/D}$ versus $(Ra_{f,L})_{Nx\times Ny,S/D}$ graph in Fig. 17. The average Nusselt number, $(Nu_{av,B})_{Nx\times Ny,S/D}$, and the modified Rayleigh number, $(Ra_{f,B})_{Nx\times Ny,S/D}$, for a rod bundle in $N_x\times N_y$ array were obtained as follows:

$$(Nu_{av,B})_{N_x\times N_y,S/D}=\sum_{i=1}^{N_x}\sum_{j=1}^{N_y}(Nu_{av})_{ij}/(N_x\times N_y) \qquad \text{for } 1\le N_x\le 9 \text{ and } 1\le N_y\le 9 \qquad (38)$$

$$(Ra_{f,L})_{N_x\times N_y,S/D}=\sum_{i=1}^{N_x}\sum_{j=1}^{N_y}(Ra_{f,L})_{ij}/(N_x\times N_y) \qquad \text{for } 1\le N_x\le 9 \text{ and } 1\le N_y\le 9 \qquad (39)$$

The numerical solutions for a vertical 9×9 rod bundle of the ESA with S/D=2 are shown as sky-blue cross symbols in the figure. And other symbols show the results for 7×7 rod bundles of the ESA with S/D=2, and vertical 5×5 rod bundles of the ESA with S/D=1.8, 2, 2.31, 3, 4, 5 and 6 [16, 18]. The numerical solutions, Nu_{av}, for the vertical single cylinder are shown in the figure for comparison as the open circles [14]. The curve-fitted numerical solutions based on the least squares method of power-law for vertical single cylinder are shown in the figure as a black solid curve for comparison. Nu_{av} values for a vertical single cylinder predicted by Eq. (18) are also shown as black dashed curves in the figure. The values given by Eqs. (26), (27) and (28) for the vertical 5×5 rod bundle with ESA are shown in Fig. 17 as colored solid lines at each ratio of the diameter of flow channel for bundle geometry to the rod diameter, S/D, for comparison. The numerical solutions for the vertical 5×5 and 7×7 rod bundles with ESA are in good agreement with the values given by the correlations, Eqs. (26), (27) and (28), within -8.90 to 2.90 % differences and -9.49 to 4.4 % ones. As can be seen from the figure, the numerical solution of $(Nu_{av,B})_{9\times9,S/D=2}$ for the vertical 9×9 rod bundle of the ESA with S/D=2 are about 67.69 % lower than the value calculated by Eq. (18) for the vertical single cylinder at the $(Ra_{f,L})_{9\times9,S/D=2}$ of 6.43×10^5 (q=2×10^5 W/m^2). They also rise linearly with the increase of $(Ra_{f,L})_{9\times9,S/D=2}$. The numerical solutions of $(Nu_{av,B})_{9\times9,S/D=2}$ for vertical 9×9 rod bundle of the ESA with S/D=2 are almost in better agreement with those of $(Nu_{av,B})_{5\times5,S/D=2}$ and $(Nu_{av,B})_{7\times7,S/D=2}$ for vertical 5×5 and 7×7 rod bundles of the ESA with S/D=2 in the whole range of the modified Rayleigh number, $(Ra_{f,B})_{Nx\times Ny,S/D=2}$, and they can be described by the authors' correlations of the vertical 5×5 rod bundle with the ESA, Eqs. (26), (27), and (28).

5.1.1 Comparison of analytical solutions ($(Nu_{av,B})_{NxxNy,S/D=2}$) for vertical 9×9 rod bundle with authors' correlations for vertical 5×5 rod bundle

The numerical solutions for a vertical 9×9 rod bundle of the ESA with S/D=2 are compared with the authors' correlations of the vertical 5×5 rod bundle, Eqs. (26), (27) and (28) in Fig. 18. The ratios of the numerical solution of the vertical 9×9 rod bundle of the ESA with S/D = 2 to the value given by the correlation, Eqs. (26), (27) and (28), are plotted as a sky-blue cross symbol on $[(Nu_{av,B})_{Nx\times Ny,S/D}]_{N\text{-}S}/[(Nu_{av,B})_{Nx\times Ny,S/D}]_{cal}$ versus $(Ra_{f,L})_{Nx\times Ny,S/D}$ graph in Fig. 18 with those for vertical 5×5 and 7×7 rod bundles [16, 18]. The authors' correlations for vertical 5×5 rod bundle are in good agreement with the numerical solutions for a vertical 9×9 rod bundle of the ESA with S/D=2 within -4.79 to 6.6 % differences as well as with the numerical solutions for vertical 5×5 and 7×7 rod bundles of the ESA with S/D=2 within -5.67 to 6.4 % differences and -9.49 to 6.4 % ones. The authors' correlations for vertical 5×5 rod bundle, Eqs. (26), (27) and (28), become the general correlations for average Nusselt number versus modified Rayleigh number, $(Nu_{av,B})_{Nx\times Ny,S/D}=f((Ra_{f,L})_{Nx\times Ny,S/D})$, from a vertical $N_x\times N_y$ rod bundle.

5.2 Effect of *S/D* on average Nusselt number

The natural convection heat transfer of a vertical 9×9 rod bundle of ESA was numerically analyzed to investigate the effect of *S/D* on heat transfer under constant heat flux conditions of $(Ra_{f,L})_{9\times9,S/D}=3.678\times10^6$ ($q=1\times10^6$ W/m^2) with *S/D* ranging from 1.82 to 5.

5.2.1 In the case of ESA

The effect of *S/D* on the average Nusselt number, $(Nu_{av,B})_{9\times9,S/D}$, from a vertical 9×9 rod bundle with ESA was estimated based on numerical *S/D* solutions ranging from 1.82 to 5. The calculations were performed for a heat flux, *q*, of 1×10^6 W/m^2 ($(Ra_{f,L})_{9\times9,S/D}=3.678\times10^6$). $(Nu_{av,B})_{9\times9,S/D}$ is shown with a light blue cross for *S/D* using array size as a parameter in Fig. 19. As can be seen from the figure, the value of $(Nu_{av,B})_{9\times9,S/D}$ at 1×10^6 W/m^2 increases linearly with *S/D* in the *S/D* range of 1.82 to 4.47, it becomes almost constant when the *S/D* becomes higher than 4.47. $(Nu_{av,B})_{5\times5,S/D}$ values (black solid square and red solid triangle symbols) for vertical 5×5 rod bundle with ESA and ETA and $(Nu_{av,B})_{7\times7,S/D}$ values (sky-blue open square symbols) for vertical 7×7 rod bundle with ESA are shown in the figure for comparison, respectively [16, 18]. The $(Nu_{av,B})_{5\times5,S/D}$ values of the vertical 5×5 rod bundle with ESA and ETA coincide with each other to form two straight lines, which can be expressed by the authors' correlations of the vertical 5×5 rod bundle with ESA and ETA, Eqs. (31) and (32), and Eqs. (33) and (34), respectively. The $(Nu_{av,B})_{9\times9,S/D}$ values for the vertical 9×9 rod bundle with ESA are almost identical to the $(Nu_{av,B})_{5\times5,S/D}$ and $(Nu_{av,B})_{7\times7,S/D}$ values for the vertical 5×5 and 7×7 rod bundles with ESA in the whole range of *S/D* and those can be expressed by authors' correlations for vertical 5×5 rod bundle with ESA, Eqs. (31) and (32), although those are a little higher at *S/D* higher than 5.

The ratios of the values of the numerical solutions of the vertical 9×9 rod bundle of the ESA with *S/D* = 1.82 to 5 to the values given by the correlations, Eqs. (31) and (32), are plotted in the $[(Nu_{av,B})_{Nx\times Ny,S/D}]_{N\text{-}S}/[(Nu_{av,B})_{Nx\times Ny,S/D}]_{cal}$ versus *S/D* graph in Fig. 20. These correlations for the vertical 5×5 rod bundle almost explain the theoretical solution for the vertical 9×9 rod bundle obtained in this study, with a difference of -4.57 to 4.94% over a wide range of *S/D*. And these authors' correlations were similarly in good agreement with the numerical solutions for a vertical 5×5 and 7×7 rod bundles of the ESA with *S/D*=1.8 to 6 within -3.36 to 1.79 % differences and -4.65 to 10.60 % ones. The author's correlations for vertical 5×5 rod bundles with ESA and ETA, Eqs. (31) and (32), and Eqs. (33) and (34), are general correlations of the average Nusselt number for *S/D*, $(Nu_{av,B})_{Nx\times Ny}$,$S/D=f(S/D)$, from vertical $N_x\times N_y$ rod bundles with ESA and ETA, respectively.

5.3 General correlations for natural convection heat transfer from vertical $N_x \times N_y$ rod bundles with S/D

In this section the correlations for natural convection heat transfer from the vertical $N_x \times N_y$ rod bundles with ESA and ETA including the effects of bundle geometry, array size, $(Ra_{f,L})_{Nx \times Ny,S/D}$ and S/D are derived based on the numerical solutions. The numerical solutions were numerically analyzed natural convection heat transfer from vertical 5×5, 7×7 and 9×9 rod bundles of ESA and ETA, with the S/D ranging from 1.8 to 6 in liquid sodium [16, 18]. The authors' correlations for vertical 5×5 rod bundle with ESA, Eqs. (26), (27) and (28), are in good agreement with the numerical solutions for vertical 5×5, 7×7 and 9×9 rod bundles of the ESA with S/D=2 at 1×10^4, 2×10^4, 7×10^4, 1×10^5, 2×10^5, 7×10^5, 1×10^6, 2×10^6 and 7×10^6 W/m^2 within -9.49 to 10.6 % differences as shown in Figs. 17 and 18. In addition, the authors' correlations of the vertical 5×5 rod bundles, Eqs. (31) and (32), almost represent the theoretical solutions obtained in this work for vertical 5×5, 7×7 and 9×9 rod bundles with ESA with S/D=1.8 to 6 at 1×10^6 W/m^2 ($(Ra_{f,L})_{Nx \times Ny,S/D}=3.678\times10^6$) : they agree well within -4.65% to 10.60 % under the wide range of S/D as shown in Figs. 19 and 20. These theoretical solutions for vertical 9×9 rod bundle of the ESA with the S/D ranging from 1.82 to 5 are plotted on $(Nu_{av,B})_{Nx \times Ny,S/D}$ versus $(Ra_{f,L})_{Nx \times Ny,S/D}$ graph in Fig. 21 as cross symbols with each color. These are also in good agreement with the values given by the correlations, Eqs. (26), (27), and (28). It is judged from these facts that the general correlations for natural convection heat transfer from vertical $N_x \times N_y$ rod bundles with ESA and ETA in liquid sodium are given by the correlations for vertical 5×5 rod bundles with the ESA, Eqs. (26), (27) and (28), and those with the ETA, Eqs. (26), (29) and (30), based on the numerical solutions as follows:

$$\left(Nu_{av,B}\right)_{N_X \times N_y,S/D} = C_1 \times (Ra_{f,L})^n_{Nx \times Ny,S/D} \times \left[\frac{1}{0.8} + \frac{C}{0.86\left(Ra_L^*\right)^{0.2}}\left(\frac{L}{D}\right)^{0.86}\right] (Ra_{f,L})^{0.2}_{N_x \times N_y,S/D} \quad \text{for } 3.08\times10^4 \le Ra_{f,L} \le 4.31\times10^7 \tag{40}$$

where

In the case of ESA:

$$C_1 = 0.00394 \times \left(\frac{S}{D}\right)^{2.47} \tag{41}$$

$$n = 0.267 - 0.0341 \times \left(\frac{S}{D}\right) \tag{42}$$

In the case of ETA:

$$C_1 = 0.00550 \times \left(\frac{S}{D}\right)^{2.52} \tag{43}$$

$$n = 0.263 - 0.0390 \times \left(\frac{S}{D}\right) \tag{44}$$

The effect of S/D on the average Nusselt number, $(Nu_{av,B})_{Nx \times Ny,S/D}$, from a vertical $N_x \times N_y$ rod bundle with the ESA and ETA is generally estimated based on the numerical solutions for the S/D ranging from 1.8 to 6 at the constant heat

flux, q, of 1×10^6 W/m^2 ($(Ra_{f,L})_{Nx\times Ny,S/D}= 3.678\times10^6$). The values of $(Nu_{av,B})_{Nx\times Ny,S/D}$ for vertical $N_x\times N_y$ rod bundles with ESA and ETA can be generally expressed by the empirical correlations:

In the case of ESA: $$\left(Nu_{av,B}\right)_{N_x\times N_y,S/D} = 2.21+24.5\times ln\left(\frac{S}{D}\right) \quad \text{for } 1.8\le S/D\le 4.47 \tag{45}$$

$$\left(Nu_{av,B}\right)_{N_x\times N_y,S/D} = Nu_{av} = 38.88 \quad \text{for } 4.47\le S/D\le 6 \tag{46}$$

In the case of ETA: $$\left(Nu_{av,B}\right)_{N_x\times N_y,S/D} = 5.89+24.5\times ln\left(\frac{S}{D}\right) \quad \text{for } 1.8\le S/D\le 3.84 \tag{47}$$

$$\left(Nu_{av,B}\right)_{N_x\times N_y,S/D} = Nu_{av} = 38.88 \quad \text{for } 3.84\le S/D\le 6 \tag{48}$$

5.4 Effect of the number of heating elements, *N*, on average Nusselt number

The numerical solutions of natural convection heat transfer for a vertical single cylinder, vertical N cylinders and vertical $N_x\times N_y$ rod bundle with the ESA and ETA were plotted in Fig. 22 to investigate the effect of the number of heating element, N, on average Nusselt number, at the constant heat flux condition of $(Ra_{f,L})_{Nx\times Ny,S/D}=3.678\times10^6$ ($q=1\times10^6$ W/m^2) for S/D of 2 and were listed in Table 4 [14-16, 18]. Further, natural convection heat transfer from vertical 3×3 rod bundle in liquid sodium was numerically analyzed to optimize the thermal-hydraulic design for the bundle geometry with ESA and ETA. The Nusselt numbers are a constant value up to two heating elements, are decreasing sharply as those increase from 2 to 9, and those become almost constant even at 9 or more as shown in Fig. 22 [14-16, 18]. When designing a Mock-up Experiment to reliably and accurately measure the typical Nusselt number, $(Nu_{av,B})_{Nx\times Ny,S/D}$, from vertical $N_x\times N_y$ rod bundle with ESA and ETA, the optimum number of heating elements in the vertical rod bundle has been clarified to be 3×3 for the first time from this figure.

6 Conclusions

Natural convection heat transfer from vertical 9×9 rod bundle in liquid sodium was numerically analyzed for the bundle geometry with ESA. For this work, a 9×9 test rod with a diameter (D = 7.6 mm), heated length (L = 200 mm), L / d (= 26.32) was used. The surface heat flux (q) of each cylinder is equally given 2×10^5 to 7×10^6 W/m^2 for the modified Rayleigh number, $(R_{f,L})_{ij}$ and $(R_{f,L})_{Nx\times Ny,S/D}$, ranging from 6.430×10^5 to 4.309×10^7 at liquid temperature (T_L = 673.15K). S/D values for rod bundles ranged from 1.82 to 5 in bundle geometry. The numerical solution leads to the following conclusions.

1) For the numerical results of $(Nu_{av})_{ij}$ on a rod bundle of a 9×9 array of an ESA with S/D=2, the 4 values at N_i=1 and 9 for N_j=1 and 9, $(Nu_{av})_{11}$, $(Nu_{av})_{19}$, $(Nu_{av})_{91}$, and $(Nu_{av})_{99}$, are near maximum. The 49 values of $(Nu_{av})_{ij}$ at N_i=2, 3, 4,

5, 6, 7 and 8 for N_j=2, 3, 4, 5, 6, 7 and 8 are almost the minimum. These 81 values of $(Nu_{av})_{ij}$ at N_i=1 to 9 for N_j=1 to 9 are considerably 14.53 to 65.12 % lower than the value for the vertical single cylinder.

2) On the $(Nu_{av})_{ij}$ versus $(N_i\text{-}1)/(N_x\text{-}1)$ and $(N_j\text{-}1)/(N_y\text{-}1)$ graphs with $(N_j\text{-}1)/(N_y\text{-}1)$ and $(N_i\text{-}1)/(N_x\text{-}1)$ as a parameter, respectively, the values of $(Nu_{av})_{ij}$ at $(N_i\text{-}1)/(N_x\text{-}1)$=0 and 1 and $(N_j\text{-}1)/(N_y\text{-}1)$=0 and 1 become higher with an increase in an array size, since the buoyancy driven flow increases. However, the 49 values of $(Nu_{av})_{ij}$ (=13.560) at $(N_i\text{-}1)/(N_x\text{-}1)$=0.125, 0.25, 0.375, 0.5, 0.625, 0.75 and 0.875 for $(N_j\text{-}1)/(N_y\text{-}1)$= 0.125, 0.25, 0.375, 0.5, 0.625, 0.75 and 0.875 on a 9×9 array are also the same with the nine values of $(Nu_{av})_{ij}$ (=12.934) at $(N_i\text{-}1)/(N_x\text{-}1)$=0.25, 0.5 and 0.75 for $(N_j\text{-}1)/(N_y\text{-}1)$=0.25, 0.5 and 0.75 on a 5×5 array and the 25 values of $(Nu_{av})_{ij}$ (=13.074) at $(N_i\text{-}1)/(N_x\text{-}1)$=0.167, 0.333, 0.5, 0.667 and 0.833 for $(N_j\text{-}1)/(N_y\text{-}1)$=0.167, 0.333, 0.5, 0.667 and 0.833 on a 7×7 array.

3) The $(Nu_{av,B})_{9\times9,S/D=2}$ for vertical 9×9 rod bundle of the ESA are almost in better agreement with the $(Nu_{av,B})_{5\times5,S/D=2}$ and $(Nu_{av,B})_{7\times7,S/D=2}$ for vertical 5×5 and 7×7 rod bundles of the ESA in the whole range of $(Ra_{f,B})_{Nx\times Ny,S/D=2}$ and they can be described by the authors' correlations, Eqs. (26), (27), and (28).

4) The effect of *S/D* on the $(Nu_{av,B})_{9\times9,S/D}$ from a vertical 9×9 rod bundle with ESA was estimated based on numerical *S/D* solutions ranging from 1.82 to 5. The $(Nu_{av,B})_{9\times9,S/D}$ values for the vertical 9×9 rod bundle with ESA are almost identical to the $(Nu_{av,B})_{5\times5,S/D}$ and $(Nu_{av,B})_{7\times7,S/D}$ values for the vertical 5×5 and 7×7 rod bundles with ESA in the whole range of *S/D* and those can be expressed by authors' correlations, Eqs. (31) and (32), although those are a little higher at *S/D* higher than 5.

5) The general correlations of natural convection heat transfer from vertical $N_x \times N_y$ rod bundles with ESA and ETA in liquid sodium are given based on the numerical solutions as follows:

$$\left(Nu_{av,B}\right)_{N_X\times N_y,S/D} = C_1 \times (Ra_{f,L})^n_{Nx\times Ny,S/D} \times \left[\frac{1}{0.8} + \frac{C}{0.86\left(Ra_L^*\right)^{0.2}}\left(\frac{L}{D}\right)^{0.86}\right](Ra_{f,L})^{0.2}_{N_X\times N_y,S/D} \quad \text{for } 3.08\times10^4 \le Ra_{f,L} \le 4.31\times10^7 \tag{40}$$

where

In the case of ESA: $$C_1 = 0.00394\times\left(\frac{S}{D}\right)^{2.47} \tag{41}$$

$$n = 0.267 - 0.0341\times\left(\frac{S}{D}\right) \tag{42}$$

In the case of ETA: $$C_1 = 0.00550\times\left(\frac{S}{D}\right)^{2.52} \tag{43}$$

$$n = 0.263 - 0.0390\times\left(\frac{S}{D}\right) \tag{44}$$

6) The effect of *S/D* on the $(Nu_{av,B})_{Nx\times Ny,S/D}$ from a vertical $N_x \times N_y$ rod bundle is generally estimated based on the numerical solutions. The $(Nu_{av,B})_{Nx\times Ny,S/D}$ for vertical $N_x \times N_y$ rod bundles with ESA and ETA can be generally expressed by the following empirical correlations:

In the case of ESA: $$\left(Nu_{av,B}\right)_{N_X\times N_y,S/D} = 2.21 + 24.5\times ln\left(\frac{S}{D}\right) \quad \text{for } 1.8 \le S/D \le 4.47 \tag{45}$$

$$\left(Nu_{av,B}\right)_{N_X\times N_y,S/D} = Nu_{av} = 38.88 \quad \text{for } 4.47 \le S/D \le 6 \tag{46}$$

In the case of ETA: $$\left(Nu_{av,B}\right)_{N_X\times N_y,S/D} = 5.89 + 24.5\times ln\left(\frac{S}{D}\right) \quad \text{for } 1.8 \le S/D \le 3.84 \tag{47}$$

$$\left(Nu_{av,B}\right)_{N_X\times N_y,S/D} = Nu_{av} = 38.88 \quad \text{for } 3.84 \le S/D \le 6 \tag{48}$$

7) When designing a Mock-up Experiment to reliably and accurately measure the typical Nusselt number, $(Nu_{av,B})_{Nx\times Ny,S/D}$, from a vertical $N_x \times N_y$ rod bundle with ESA and ETA, the optimum number of heating elements in the vertical rod bundle has been clarified to be 3×3 for the first time.

Nomenclature

C	parameters in Eqs. (13), (18), (26) and (40)
C_1	parameters in Eqs. (26), (27), (29), (40), (41) and (43)
c_p	specific heat at constant pressure, J/kg K
D	cylinder diameter and rod diameter, m
Gr_L^*	$= g\,\beta_l\,q\,L^4/\lambda_l\,\nu_l^2$, Grashof number for constant heat flux
Gr_z^*	$= g\,\beta_l\,q\,z^4/\lambda_l\,\nu_l^2$, local Grashof number for constant heat flux
g	acceleration of gravity, m/s^2
H	liquid head and height on calculation domain, m
L	heated length, m
l	depth on calculation domain, m
n	exponents in Eqs. (26), (28), (30), (40), (42) and (44)
N	number of heating element
N_x	column number
N_y	row number
Nu	Nusselt number
$(Nu_{av})_{ij}$	average Nusselt number for vertical single cylinder

$(Nu_{av,B})_{5\times5,S/D}$ average Nusselt number for the vertical 5×5 rod bundle with various *S/D*

$(Nu_{av,B})_{7\times7,S/D}$ average Nusselt number for the vertical 7×7 rod bundle with various *S/D*

$(Nu_{av,B})_{9\times9,S/D}$ average Nusselt number for the vertical 9×9 rod bundle with various *S/D*

$(Nu_{av,B})_{N,S/D}$ average Nusselt number for the vertical rod bundle with various *S/D*

$(Nu_{av,B})_{Nx\times Ny,S/D}$ average Nusselt number for the vertical $N_x \times N_y$ rod bundle with various *S/D*

Nu_z $=q\ z/\lambda_l\ (T_S-T_L)$, local Nusselt number for a vertical cylinder

P System pressure, kPa

Pr $=cp_l\ \mu_l/\lambda_l$, Prandtl number

$(Pr)_{TEM}$ Prandtl number evaluated at calculated temperature of the first control volume on the heated surface

$(Pr)_{TEM,av}$ Prandtl number evaluated at the average calculated temperature of the first control volume on the heated surface

Ra_L^* $= Gr_L^*Pr$, Rayleigh number for constant heat flux

Ra_z^* $= Gr_z^*Pr$, local Rayleigh number for constant heat flux

Ra_f $= Gr_z^*Pr^2/(4+9Pr^{1/2}+10Pr)$, modified local Rayleigh number

$Ra_{f,L}$ $= Gr_L^*Pr^2/(4+9Pr^{1/2}+10Pr)$, modified Rayleigh number

$(Ra_{f,L})_{ij}$ $= (Gr_L^*)_{ij}(Pr)_{ij}^2/\{4+9(Pr)_{ij}^{1/2}+10(Pr)_{ij}\}$, modified Rayleigh number for vertical single cylinder

$(Ra_{f,L})_{5\times5,S/D}$ $= (Gr_L^*)_{5\times5,S/D}(Pr)_{5\times5,S/D}^2/\{4+9(Pr)_{5\times5,S/D}^{1/2}+10(Pr)_{5\times5,S/D}\}$, modified Rayleigh number for the vertical 5×5 rod bundle with various *S/D*

$(Ra_{f,L})_{7\times7,S/D}$ $= (Gr_L^*)_{7\times7,S/D}(Pr)_{7\times7,S/D}^2/\{4+9(Pr)_{7\times7,S/D}^{1/2}+10(Pr)_{7\times7,S/D}\}$, modified Rayleigh number for the vertical 7×7 rod bundle with various *S/D*

$(Ra_{f,L})_{9\times9,S/D}$ $= (Gr_L^*)_{9\times9,S/D}(Pr)_{9\times9,S/D}^2/\{4+9(Pr)_{9\times9,S/D}^{1/2}+10(Pr)_{9\times9,S/D}\}$, modified Rayleigh number for the vertical 9×9 rod bundle with various *S/D*

$(Ra_{f,L})_{Nx\times Ny,S/D}$ $= (Gr_L^*)_{Nx\times Ny,S/D}(Pr)_{Nx\times Ny,S/D}^2/\{4+9(Pr)_{Nx\times Ny,S/D}^{1/2}+10(Pr)_{Nx\times Ny,S/D}\}$, modified Rayleigh number for the vertical $N_x \times N_y$ rod bundle with various *S/D*

r radius of a cylinder, m

Δr first control volume width for *r*-component, m

S diameter of flow channel for bundle geometry and distance between center axes, mm

T temperature, K

TEM calculated temperature of the first control volume on the heated surface, K

TEM_{av} average calculated temperature of the first control volume on the heated surface, K

T_f liquid temperature, K

T_0 bulk liquid temperature, K

T_L bulk liquid temperature, K

T_s heater surface temperature, K

$T_{s,av}$ average surface temperature, K

$(T_s)_z$ local surface temperature, K

ΔT_L $=T_{s,av}-T_L$, average surface temperature and liquid bulk mean temperature, K

t time, s

Δt time step, s

u velocity component in x-direction, m/s

v velocity component in y-direction, m/s

w velocity component in z-direction, m/s, and width of calculation domain, m

x Cartesian coordinate, m

Δx Δr-component in x-direction, m

y Cartesian coordinate, m

Δy Δr-component in y-direction, m

z Cartesian coordinate, cylinder height and the vertical distance from the leading edge of the heated section, m

Greek Letters

β volumetric expansion coefficient, K^{-1}

δ_{CSL} $= (\Delta r)_{out}/2$, thickness of local conductive sub-layer, m

$\delta_{CSL,av}$ $=(\Delta r)_{out}/2$, thickness of average conductive sub-layer on forced convection, m

δ_{VSL} thickness of local viscous sub-layer on forced convection, m

$\delta_{VSL,av}$ thickness of average viscous sub-layer on forced convection, m

θ peripheral angle from inside on the r-θ plane

λ thermal conductivity, W/(m K)

μ viscosity, Ns/m^2

v kinematic viscosity, m^2/s

ρ density, kg/m^3

Acronyms and abbreviations

CFD Computational Fluid Dynamics

ESA equilateral square array

ETA equilateral triangle array

PHOENICS parabolic hyperbolic or elliptic numerical integration code series

S/D ratio of the diameter of flow channel for bundle geometry to the rod diameter

SIMPLE Semi-Implicit Method for Pressure-Linked Equations

Subscript

l liquid

Acknowledgments

This work was supported by the "Joint Usage/Research Program on Zero-Emission Energy Research, Institute of Advanced Energy, Kyoto University, Japan, ZE29B-10, 2017, ZE30B-03, 2018 and ZE31B-05, 2019."

References

[1] Dutton, J.C., 1975. An experimental investigation of natural convection heat transfer from an array of uniformly heated vertical cylinders to mercury, Thesis of Master of Science, Oregon State University, Corvallis, OR, USA, 179 pages.

[2] Cheng, S.K. and Todreas, N.E., 1986. Hydrodynamic Models and Correlations for Bare and Wire-wrapped Hexagonal Rod Bundle Friction Factors, Subchannel Friction Factors and mixing Parameters, Nuclear Engineering and Design, Vol. 92, pp. 227-512.

[3] Ninokata, H., Efthimiadis, A. and Todreas, N.E., 1987. Distributed resistance modeling of wire-wrapped rod bundles, Nuclear Engineering and Design, Vol. 104, pp. 93-102.

[4] Gajapathy, R., Velusamy, K., Selvaraj, P., Chellapandi P. and Chetal S.C., 2007. CFD investigation of helical wire-wrapped 7-pin fuel bundle and the challenges in modeling full scale 217 pi bundle, Nuclear Engineering and Design, Vol. 237, pp. 2332-2342.

[5] Rolfo, S., Peniguel, C., Guillaud, M. and Laurence, D., 2012. Thermal-hydraulic study of a wire spacer fuel assembly, Nuclear Engineering and Design, Vol. 243, pp. 251-262.

[6] Merzari, E., Pointer, W.D., Smith, J.G., Tentner, A. and Fischer, P., 2012. Numerical simulation of the flow in wire-wrapped pin bundles: Effect of pin-wire contact modeling, Nuclear Engineering and Design, Vol. 253, pp. 374-386.

[7] Hu, R. and Fanning, T.H., 2013. A momentum source model for wire-wrapped rod bundles—Concept, validation, and application, Nuclear Engineering and Design, Vol. 262, pp. 371-389.

[8] Roelofs, F., Gopala, V.R., Jayaraju, S., Shams, A. and Komen, E., 2013. Review of fuel assembly and pool thermal hydraulics for fast reactors, Nuclear Engineering and Design, Vol. 265, pp. 1205-1222.

[9] Raj, M.N. and Velusamy, K., 2016. Characterization of velocity and temperature fields in a 217 pin wire wrapped fuel bundle of sodium cooled fast reactor, Annuls of Nuclear Energy, Vol. 87, pp. 331-349.

[10] Hata K., Takeuchi Y., Shiotsu M., Sakurai A., 1999, Natural convection heat transfer from a horizontal cylinder in liquid sodium (Part 1: Experimental results), *Nuclear Engineering and Design*, Vol.193, pp. 105-118.

[11] Hata K., Takeuchi Y., Shiotsu M., Sakurai A., 1999, Natural convection heat transfer from a horizontal cylinder in liquid sodium (Part 2: Generalized correlation for laminar natural convection heat transfer), *Nuclear Engineering and Design*, Vol.194, pp. 185-196.

[12] Hata K., Takeuchi Y., Hama K. and Shiotsu M., 2015, Natural convection heat transfer from horizontal Rod bundles in liquid sodium Part 1: Correlations for two parallel horizontal cylinders based on experimental and theoretical results, *Journal of Nuclear Science and Technology*, Vol. 52, No.2, pp. 214-227.

[13] Hata K., Takeuchi Y., Hama K. and Shiotsu M., 2015, Natural convection heat transfer from horizontal Rod bundles in liquid sodium Part 2: Correlations for horizontal rod bundles based on theoretical results, *Journal of Nuclear Science and Technology*, Vol. 52, No.3, pp. 342-354.

[14] Hata K., Takeuchi Y., Hama K., Shiotsu M., Shirai Y. and Fukuda K., 2014, Natural convection heat transfer from a vertical cylinder in liquid sodium, *Mechanical Engineering Journal*, Vol. 1, No. 1, pp. 1-12.

[15] Hata K., Fukuda K. and Mizuuchi T., 2016, Natural Convection Heat Transfer from Vertical Rod Bundles in Liquid Sodium, *Mechanical Engineering Journal*, Vol. 3, No. 3, pp. 1-16.

[16] Hata K., K. Fukuda K. and Mizuuchi T., 2017, Natural Convection Heat Transfer from Vertical 5×5 Rod Bundles in Liquid Sodium, *Journal of Heat Transfer,* Trans. ASME, Vol. 139, pp. 032502-1-11.

[17] Hata K., Liu Q. S. and Nakajimai T., 2019, Natural Convection Heat Transfer from a Vertical Single Cylinder with Helical Wire Spacer in Liquid Sodium, *Nuclear Engineering and Design*, Vol. 341, pp. 73-90.

[18] Hata K., Fukuda K. and Mizuuchi T., 2019, Laminar Natural Convection Heat Transfer from Vertical 7×7 Rod Bundles in Liquid Sodium, *Journal of Nuclear Engineering and Radiation Science*, Trans. ASME, Vol. 5, pp. 021002-1-15.

[19] Patankar, S.V., 1980, “Numerical Heat Transfer and Fluid Flow,” Hemisphere Pub. Corp..

[20] Favre-Marinet, Michel, and Tardu, Sedat, 2009, "*Convective Heat Transfer*," ISTE Ltd and John Wiley & Sons, Inc., Great Britain and United States.

[21] Hanjalic, K., Kenjeres, S., Tummers, M.J., and Jonker, H.J.J., 2009, "*Analysis and Modeling of Physical Transport Phenomena*," Published by VSSD.

[22] Spalding, D.B., 1991, “The PHOENICS Beginner's Guide,” Pub. by CHAM, UK.

[23] LeFevre, E.J., and Ede, A.J., 1957, "Laminar Free Convection from the Outer Surface of a Vertical Circular Cylinder," *Proceedings of the 9th International Congress on Applied Mechanics Brussels*, Vol. 4, pp.175-183.

[24] Mabuchi, I., 1961, "Laminar Free Convection from a Vertical Cylinder with Uniform Surface Heat Flux," *Trans. Jpn. Soc. Mech. Eng.*, Vol. 27, No. 180, (in Japanese), pp. 1306-1313.

[25] Louis C. Burmeister, 1983, "Convective Heat Transfer," *John Willy & Sons*, p. 536.

APPENDIX A

A.1. Thicknesses of local conductive and viscous sub-layers, δ_{CSL} and δ_{VSL}, on laminar natural convection heat transfer

Figures 23, 24 and 25 show the experimental results of local and average surface temperature rises, $(Ts)_z$-T_L and $T_{s,av}$-T_L, against the *z*-axis distance from the leading edge of the heated section for the liquid temperatures ranged from 766 to 798 K at the heat fluxes, *q*, of 0.7, 1.0 and 2.0 MW/m^2, respectively [14, 15]. In these figures, T_s-T_L are shown by black solid triangles, $T_{s,av}$-T_L: are shown by black open triangles, and *q* are shown by black solid lines. The average surface temperature rises, $T_{s,av}$-T_L, was determined from the arithmetic mean of the measured local surface temperature rises on the heated surface and displayed at the midpoint of the heated length (*z*=98 mm) with a black open triangle symbol.

The numerical solutions of the *z*-axis variations in the analyzed liquid temperature rises of the outer control volume on the heated surface, *TEM*-T_L, are shown at the heat fluxes of 0.7, 1.0 and 2.0 MW/m^2 in the liquid temperature of 773.15 K as a green broken line in each figure. The numerical solutions of the local surface temperature rises on the heated surface, $(T_s)_z$-T_L, were analyzed from the calculated temperature of the first control volume on the heated surface, *TEM*, which is located at the center of the control volume, by solving the liquid heat conduction equation given by Eq. (12). The *z*-axis variations in the local surface temperature rises of the test cylinder at every 5 mm in the heated length, *L*, are shown as a black solid line with green circle in the figure. They become gradually higher with an increase in the *z*-axis distance from the leading edge of the heated section. The average values of numerical solution of the local surface temperature rise ($T_{s,av}$-T_L:green solid circle) solved by the theoretical equations for laminar heat transfer, Eqs. (1) to (12), almost agree with the experimental result ($T_{s,av}$-T_L: black open triangle) determined from the arithmetic mean of the measured local surface temperatures on the heated surface within +11.68 % difference. The thickness of the local conductive sub-layer, δ_{CSL}, for the laminar natural convection heat transfer on the test cylinder of *D*=7.6 mm and *L*=186 mm is 200 μm at the heat fluxes of 0.7, 1.0 and 2.0 MW/m^2 in liquid temperature, T_L, of 773.15 K as shown in Figs. 23, 24 and 25. The thickness of the local conductive sub-layer does not depend on the surface heat flux and the heater surface temperature, and that is a constant value 200 μm in the wide *z* region. The thickness of local conductive

sub-layer, δ_{CSL}, at various z are shown as a red solid line in Fig. 23, 24 and 25 with q=0.7, 1.0 and 2.0 MW/m^2 and are listed in Table 5, 6 and 7, respectively. The thickness of the local conductive sublayer is a constant value 200 μm for a wide range of heat fluxes and surface temperatures.

The Prandtl numbers evaluated at the calculated temperature of the first control volume on the heated surface, *TEM*, and thicknesses of local viscous sub-layer at various z are shown as a blue solid line and a red broken line in Figs. 23, 24 and 25 with q=0.7, 1.0 and 2.0 MW/m^2, respectively, and are also listed in Tables 5, 6 and 7. Results of scale analysis in laminar thermal boundary layers give the order of magnitude of the main values shown in following equations [20, 21]:

$$\delta_{VSL}/\delta_{CSL} = Pr^{1/2} \quad \text{for } Pr<<1 \tag{49}$$

$$\delta_{VSL}/\delta_{CSL} = 1 \quad \text{for } Pr=1 \tag{50}$$

$$\delta_{VSL}/\delta_{CSL} = Pr^{1/3} \quad \text{for } Pr>1 \tag{51}$$

The calculated temperatures of the first control volume on the heated surface, *TEM*, become higher as z becomes larger, but the Prandtl numbers evaluated at *TEM*, $(Pr)_{TEM}$, decrease gradually with an increase in z and those become smaller as the heat flux becomes larger. The thickness of the local viscous sub-layer, δ_{VSL}, for the laminar natural convection heat transfer on the test cylinder of D=7.6 mm and L=186 mm are estimated from Eq. (49) with the thickness of the local conductive sub-layer and Prandtl number evaluated at *TEM*. These thicknesses of the local viscous sub-layer, δ_{VSL}, are 13.485 to 13.316 μm, 13.399 to 13.179 μm and 13.155 to 12.834 μm in the wide range of the heater surface temperature rises, $(T_s)_z$-T_L, at q=0.7, 1.0 and 2.0 MW/m^2, respectively. The thickness of the local viscous sub-layer decreases gradually with an increase in the z-axis distance from the leading edge of the heated section with a decreasing trend similar to Prandtl number, $(Pr)_{TEM}$.

And the average values of the thicknesses of the local viscous sub-layer become 13.3665 μm, 13.2443 μm and 12.9261 μm at q=0.7, 1.0 and 2.0 MW/m^2 as shown by a red solid inverted triangle symbol at z=96 mm in Figs. 23, 24 and 25, respectively, while those of the thicknesses of the local conductive sub-layer become 200 μm as shown by a red solid triangle symbol. It has been confirmed from these facts that the thickness of the local conductive sub-layer is constant even over a wide range of heat flux and local surface temperature of the test cylinder while the thickness of the local viscous sub-layer vary gradually depending on the heat flux and the surface temperature. The thickness of the average conductive sub-layer is always the same as the thickness of the local conductive sub-layer regardless of the heat flux and the local surface temperature.

APPENDIX A

A.1. Thicknesses of local conductive and viscous sub-layers, δ_{CSL} and δ_{VSL}, on laminar natural convection heat transfer

Figure and Table Captions

Table 1 Number of heating elements used in the experimental and numerical studies of natural convection heat transfer from rod bundle in liquid metals that have been reported so far.

Fig. 1 1/2 model of a vertical 9×9 rod bundle test vessel.

Fig. 2 Top view of vertical 9×9 rod bundle with ESA.

Fig. 3 Boundary fitted coordinates: ESA (a and b).

Fig. 4 Liquid temperature of conductive sublayer based on numerically predicted data (solution of unsteady laminar three-dimensional fundamental equation) for a vertical single cylinder with a diameter of 7.6 mm [14-18, 20, 21].

Fig. 5 Experimental data on the local surface temperature rise, $(T_s)_z$-T_L, of a vertical single test cylinder versus the vertical distance from the leading edge of the heated section, z, at heat fluxes of 2×10^5 to 2×10^6 W/m^2 [14] compared with the numerical solutions and Eq. (13).

Fig. 6 Heat transfer process (q vs. ΔT_L) on the vertical cylinder, thicknesses of average conductive and viscous sub-layers, and Prandtl numbers evaluated at TEM_{av}, $(Pr)_{TEM,av}$.

Table 2 Thicknesses of average conductive and viscous sub-layers, $\delta_{CSL,av}$ and $\delta_{VSL,av}$, and Prandtl numbers evaluated at the average calculated temperature of the first control volume on the heated surface under laminar natural convection, $(Pr)_{TEN,av}$, at various ΔT_L.

Fig. 7 The relationship between Prandtl number and sodium temperature.

Fig. 8 Theoretical solution, $(Nu_{av,B})_{Nx\times Ny,S/D}$, for vertical 5×5 and 7×7 rod bundles with ESA, Eqs. (26), (27) and (28), and correlation for vertical single cylinder [14-16, 18].

Fig. 9 Average Nusselt number, $(Nu_{av,B})_{Nx\times Ny,S/D}$, for vertical 5×5 and 7×7 rod bundles with ESA and ETA versus the S/D at $(Ra_{f,L})_{Nx\times Ny,S/D}=3.54\times10^6$ (q =1×10^6 W/m^2) [14-16, 18].

Table 3 Parameters used for the calculation.

Fig. 10 $(Nu_{av})_{ij}$ versus N_x of a vertical 9×9 rod bundle with ESA with N_y as a parameter at $(Ra_{f,L})_{ij}$= 3.678×10^6 (q = 1×10^6 W/m^2).

Fig. 11 $(Nu_{av})_{ij}$ versus N_y of a vertical 9×9 rod bundle with ESA with N_x as a parameter at $(Ra_{f,L})_{ij}$= 3.678×10^6 (q = 1×10^6 W/m^2).

Fig. 12 $(Nu_{av})_{ij}$ versus $(N_i\text{-}1)/(N_x\text{-}1)$ of vertical 5×5, 7×7 and 9×9 rod bundles of ESA with $(N_j\text{-}1)/(N_y\text{-}1)$ as a parameter at $(Ra_{f,L})_{ij}=3.678\times10^6$ (q = 1×10^6 W/m^2) [14-16, 18].

Fig. 13 $(Nu_{av})_{ij}$ versus $(N_j\text{-}1)/(N_y\text{-}1)$ of vertical 5×5, 7×7 and 9×9 rod bundles of ESA with $(N_i\text{-}1)/(N_x\text{-}1)$ as a parameter at $(Ra_{f,L})_{ij}$= 3.678×10^6 (q = 1×10^6 W/m^2) [14-16, 18].

Fig. 14 Liquid temperature contours in the *x*-*y* plane at *z* = 25, 95, and 195 mm (*iz* = 11, 18 and 28) for a vertical 9×9 rod bundle of an ESA with *S*/*D* = 2 at $(Ra_{f,L})_{9\times9,S/D=2}$= 3.678×10^6 ($q$= 1×10^6 W/m^2).

Fig. 15 Liquid temperature contours at the *x*-*z* plane on *iy*=127 and at the *y*-*z* plane on *ix*=1 for vertical 9×9 rod bundle of ESA with *S*/*D* = 2 at $(Ra_{f,L})_{9\times9,S/D=2}$ =3.678×10^6 (q=1×10^6 W/m^2).

Fig. 16 Distribution of velocity vector of the *x*-*y* plane on *iz*=1, 11, 18, 28 and 37 for vertical 9×9 rod bundle of ESA at *S*/*D* = 2at $(Ra_{f,L})_{9\times9,S/D=2}$= 3.678×10^6 ($q$=1×10^6 W/m^2).

Fig. 17 Theoretical solutions of $(Nu_{av,B})_{9x9,S/D=2}$ for vertical 9×9 rod bundle of ESA with *S*/*D*=2, $(Nu_{av,B})_{7x7,S/D=2}$ for vertical 7×7 rod bundle of ESA with *S*/*D*=2 [18] and $(Nu_{av,B})_{5x5,S/D}$ for vertical 5×5 rod bundle of ESA with *S*/*D*=1.8 to 6 [16], and Nu_{av} for vertical single cylinder [14].

Fig. 18 Comparison of theoretical solutions of $(Nu_{av,B})_{9x9,S/D=2}$ for vertical 9×9 rod bundle of ESA, $(Nu_{av,B})_{7x7,S/D=2}$ for vertical 7×7 rod bundle of ESA [18] and $(Nu_{av,B})_{5x5,S/D=2}$ for vertical 5×5 rod bundle of ESA [16] with authors' correlations, Eqs. (26), (27) and (28).

Fig. 19 Average Nusselt number of $(Nu_{av,B})_{Nx\times Ny,S/D}$ for the ESA and ETA versus the *S*/*D* at $(Ra_{f,L})_{Nx\times Ny,S/D}$=3.678×10^6 ($q$ =1×10^6 W/m^2) [16, 18].

Fig. 20 Comparison of theoretical solutions of $(Nu_{av,B})_{9x9,S/D}$ for vertical 9×9 rod bundle of ESA, $(Nu_{av,B})_{7x7,S/D}$ for vertical 7×7 rod bundle of ESA [18] and $(Nu_{av,B})_{5x5,S/D}$ for vertical 5×5 rod bundle of ESA [16] with authors' correlations, Eqs. (31) and (32).

Fig. 21 Theoretical solutions of $(Nu_{av,B})_{Nx\times Ny,S/D}$ for vertical 9×9 rod bundle with ESA from *S*/*D*=1.82 to 5, $(Nu_{av,B})_{7x7,S/D}$ for vertical 7×7 rod bundle with ESA from *S*/*D*=1.8 to 6 [18], $(Nu_{av,B})_{5x5,S/D}$ for vertical 5×5 rod bundle with ESA from *S*/*D*=1.8 to 6 [16], and the Nu_{av} and the correlation for vertical single cylinder [14, 15].

Fig. 22 Average Nusselt number, Nu_{av}, $(Nu_{av,B})_{N,S/D=2}$ and $(Nu_{av,B})_{Nx\times Ny,S/D=2}$, for the ESA and ETA versus the heating element number, *N*, at $(Ra_{f,L})_{Nx\times Ny,S/D=2}$=3.678×10^6 ($q$ =1×10^6 W/m^2) [14-16, 18].

Table 4 Nu_{av} for a vertical single cylinder, $(Nu_{av,B})_{N,S/D=2}$ for vertical *N* cylinders and $(Nu_{av,B})_{Nx\times Ny,S/D=2}$ for vertical $N_x\times N_y$ rod bundle with the ESA and ETA [14-16, 18].

Fig. 23 Local and average surface temperatures at 0.7 MW/m^2 for vertical single test cylinder against the vertical distance from the leading edge of the heated section, *z*, compared with numerical solutions of *TEM*-T_L, local and average surface temperature rises numerically analyzed by δ_{CSL}=200 μm, and δ_{VSL}, $(Pr)_{TEM}$ evaluated at *TEM* on laminar natural convection.

Table 5 Thicknesses of local conductive and viscous sub-layers, δ_{CSL} and δ_{VSL}, and $(Pr)_{TEM}$ evaluated at *TEM* on laminar natural convection heat transfer for various T_s with q=0.7 MW/m^2.

Fig. 24 Local and average surface temperatures at 1.0 MW/m^2 for vertical single test cylinder against the vertical distance from the leading edge of the heated section, *z*, compared with numerical solutions of *TEM*-T_L, local and average surface temperature rises numerically analyzed by δ_{CSL}=200 μm, and δ_{VSL}, $(Pr)_{TEM}$ evaluated at *TEM* on laminar natural convection.

Table 6 Thicknesses of local conductive and viscous sub-layers, δ_{CSL} and δ_{VSL}, and $(Pr)_{TEM}$ evaluated at *TEM* on laminar natural convection heat transfer for various T_s with q=1.0 MW/m^2.

Fig. 25 Local and average surface temperatures at 2.0 MW/m^2 for vertical single test cylinder against the vertical distance from the leading edge of the heated section, *z*, compared with numerical solutions of *TEM*-T_L, local and average surface temperature rises numerically analyzed by δ_{CSL}=200 μm, and δ_{VSL}, $(Pr)_{TEM}$ evaluated at *TEM* on laminar natural convection.

Table 7 Thicknesses of local conductive and viscous sub-layers, δ_{CSL} and δ_{VSL}, and $(Pr)_{TEM}$ evaluated at *TEM* on laminar natural convection heat transfer for various T_s with q=2.0 MW/m^2.

Table 1 Number of heating elements used in the experimental and numerical studies of natural convection heat transfer from rod bundle in liquid metals that have been reported so far.

Reference	Fluid	Method	Number of Heating Elements
Dutton, 1975 [1]	Mercury	Experiment	7 pins
Cheng and Todreas, 1986 [2]	Sodium, Water and Molten Salt	Experiment	37 pins
Ninokata et al., 1987 [3]	Sodium	Experiment	19 pins
Gajapathy et al., 2007 [4]	Sodium	Experiment	7 pins
		CFD Simulation	7 and 217 pins
Rolfo et al., 2012 [5]	Liquid Metal	CFD Simulation	7, 19, 61 and 271 pins
Merzari et al., 2012 [6]	Sodium	CFD Simulation	217 pins
Hu and Fanning, 2013 [7]	Sodium	Experiment	61 pins
		CFD Simulation	7 and 37 pins
Roelofs et al., 2013 [8]	Water	Experiment	7 pins
	Liquid Metal	CFD Simulation	7 pins
Raj and Velusamy, 2016 [9]	Sodium	CFD Simulation	217 pins
Hata et al., 1999 [10]	Sodium	Experiment	1 pin
Hata et al., 1999 [11]	Sodium	CFD Simulation	1 pin
Hata et al., 2015 [12]	Sodium	Experiment	2 pins
		CFD Simulation	2, 5 and 9 pins
Hata et al., 2015 [13]	Sodium	CFD Simulation	5×5, 7×7 and 9×9 pins
Hata et al., 2015 [14]	Sodium	Experiment	1 pin
		CFD Simulation	1 pin
Hata et al., 2016 [15]	Sodium	CFD Simulation	2, 3 and 4 pins
Hata et al., 2017 [16]	Sodium	CFD Simulation	5×5 pins
Hata et al., 2019 [17]	Sodium	CFD Simulation	1 pin with wire spacer
Hata et al., 2019 [18]	Sodium	CFD Simulation	7×7 pins

Table 2 Thicknesses of average conductive and viscous sub-layers, $\delta_{CSL,av}$ and $\delta_{VSL,av}$, and Prandtl numbers evaluated at the average calculated temperature of the first control volume on the heated surface under laminar natural convection, $(Pr)_{TEM,av}$, at various ΔT_L.

ΔT_L (K)	18.726	56.801	78.014	145.023
$(Pr)_{TEM,av}$	0.0046294	0.0044662	0.0043845	0.0041735
$\delta_{CSL,av}$ (μm)	200	200	200	200
$\delta_{VSL,av}$ (μm)	13.6080	13.3659	13.2430	12.9206

Table 3 Parameters used for the calculation.

System Pressure (P) [kPa]	101.3				
Rod diameter, Cylinder Diameter (D) [mm]	7.6				
Heated Length (L) [mm]	200				
Heating element number (N)	81 (9×9) heating elements				
Bundle geometry	ESA				
S/D (S=diameter of flow channel for bundle geometry)	1.82	2	3	4	5
Liquid Temperature (T_L) [K]	673	673	673	673	673
Heat Flux (q) [W/m^2]	2×10^5	7×10^5	1×10^6	2×10^6	7×10^6
Gr_L^*	1.307×10^{11}	5.294×10^{11}	8.115×10^{11}	1.963×10^{12}	1.250×10^{13}
Ra_L^* ($=Gr_L^*Pr$)	6.264×10^8	2.432×10^9	3.657×10^9	8.447×10^9	4.981×10^{10}
$(Ra_{f,L})_{Nx\times Ny,S/D}$ $\{=Gr_L^*Pr^2/(4+9Pr^{1/2}+10Pr)\}$	6.430×10^5	2.401×10^6	3.678×10^6	7.855×10^6	4.309×10^7
First Control Volume Width for r-component (Δr) [mm]	0.4				
Thickness of the average conductive sub-layer ($\delta_{CSL,av}$) [μm]	200				
Coordinate system	Boundary fitted coordinates (x, y, z)				
Control volume number	(100, 257, 37)				
Physical model	Laminar model				

Table 4 Nu_{av} for a vertical single cylinder, $(Nu_{av,B})_{N,S/D=2}$ for vertical N cylinders and $(Nu_{av,B})_{Nx\times Ny,S/D=2}$ for vertical $N_x\times N_y$ rod bundle with the ESA and ETA [14-16, 18].

N	1	2	3	4 (2×2)	9 (3×3)	25 (5×5)	49 (7×7)	81 (9×9)
Nu_{av} $(Nu_{av,B})_{N,S/D=2}$ $(Nu_{av,B})_{Nx\times Ny,S/D=2}$ with ETA	38.878 (1)	39.197 (1.0082)	34.268 (0.8814)		24.6549 (0.6342)	23.0845 (0.5938)		
Nu_{av} $(Nu_{av,B})_{N,S/D=2}$ $(Nu_{av,B})_{Nx\times Ny,S/D=2}$ with ESA				29.690 (0.7637)	20.6596 (0.5314)	19.2054 (0.4940)	18.8577 (0.4850)	18.9791 (0.4882)

Table 5 Thicknesses of local conductive and viscous sub-layers, δ_{CSL} and δ_{VSL}, and $(Pr)_{TEM}$ evaluated at *TEM* on laminar natural convection heat transfer for various T_s with q=0.7 MW/m^2.

z (mm)	7.5	32.5	57.5	82.5	107.5	132.5	157.5	183.
T_s (K)	811.585	823.856	828.508	831.430	833.580	835.287	836.707	838.038
$(Pr)_{TEM}$	0.004546	0.004492	0.004472	0.004460	0.004451	0.004444	0.004438	0.004433
δ_{CSL} (μm)	200	200	200	200	200	200	200	200
δ_{VSL} (μm)	13.4845	13.4046	13.3750	13.3567	13.3433	13.3327	13.3240	13.3159

Table 6 Thicknesses of local conductive and viscous sub-layers, δ_{CSL} and δ_{VSL}, and $(Pr)_{TEM}$ evaluated at *TEM* on laminar natural convection heat transfer for various T_s with q=1.0 MW/m^2.

z (mm)	7.5	32.5	57.5	82.5	107.5	132.5	157.5	183.
T_s (K)	825.732	842.621	849.095	853.185	856.200	858.599	860.596	862.470
$(Pr)_{TEM}$	0.004488	0.004418	0.004392	0.004377	0.004365	0.004356	0.004349	0.004342
δ_{CSL} (μm)	200	200	200	200	200	200	200	200
δ_{VSL} (μm)	13.3985	13.2938	13.2552	13.2313	13.2139	13.2003	13.1890	13.1785

Table 7 Thicknesses of local conductive and viscous sub-layers, δ_{CSL} and δ_{VSL}, and $(Pr)_{TEM}$ evaluated at *TEM* on laminar natural convection heat transfer for various T_s with q=2.0 MW/m^2.

z (mm)	7.5	32.5	57.5	82.5	107.5	132.5	157.5	183.
T_s (K)	869.979	901.471	913.923	921.882	927.785	932.500	936.434	940.108
$(Pr)_{TEM}$	0.004326	0.004222	0.004185	0.004164	0.004148	0.004136	0.004127	0.004118
δ_{CSL} (μm)	200	200	200	200	200	200	200	200
δ_{VSL} (μm)	13.1546	12.9949	12.9388	12.9051	12.8812	12.8627	12.8478	12.8342

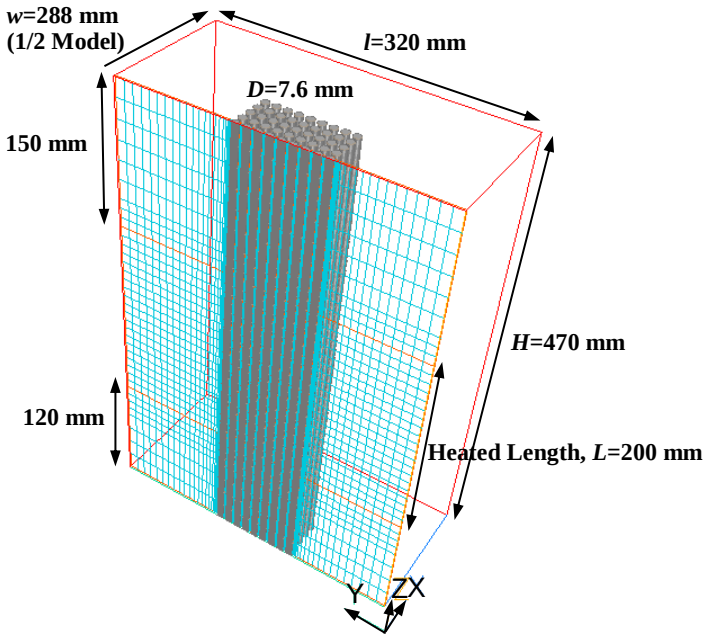

Fig. 1 1/2 model of a vertical 9×9 rod bundle test vessel

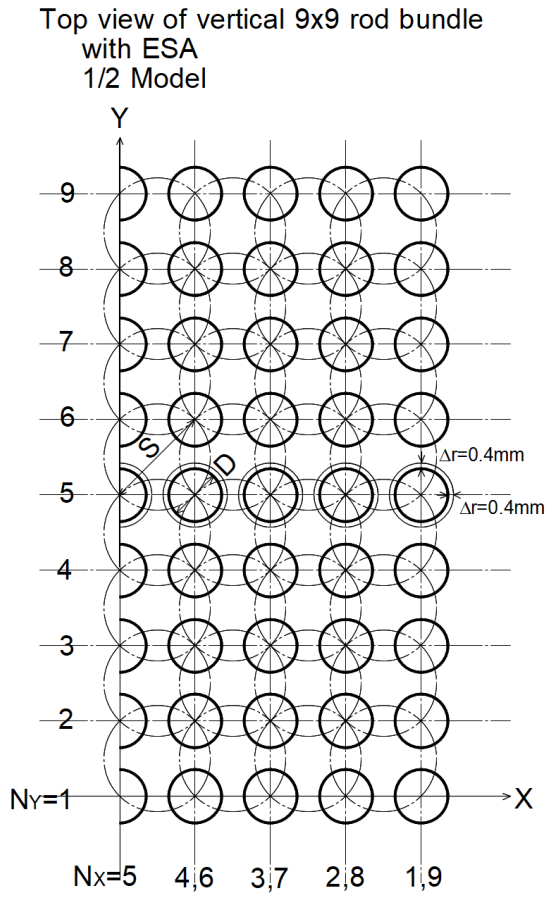

Fig. 2 Top view of vertical 9×9 rod bundle with ESA.

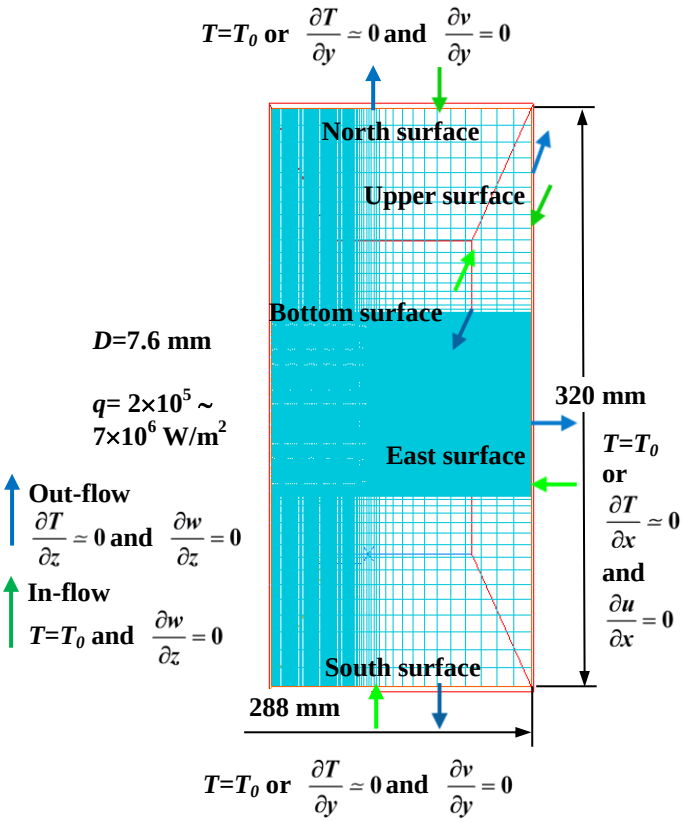
$T=T_0$ or $\frac{\partial T}{\partial y} \simeq 0$ and $\frac{\partial v}{\partial y} = 0$
North surface
Upper surface
Bottom surface
East surface
South surface
D=7.6 mm
q= 2×10^5 ~ 7×10^6 W/m^2
320 mm
$T=T_0$ or $\frac{\partial T}{\partial x} \simeq 0$ and $\frac{\partial u}{\partial x} = 0$
Out-flow
$\frac{\partial T}{\partial z} \simeq 0$ and $\frac{\partial w}{\partial z} = 0$
In-flow
$T=T_0$ and $\frac{\partial w}{\partial z} = 0$
288 mm
$T=T_0$ or $\frac{\partial T}{\partial y} \simeq 0$ and $\frac{\partial v}{\partial y} = 0$

(a) (ESA)

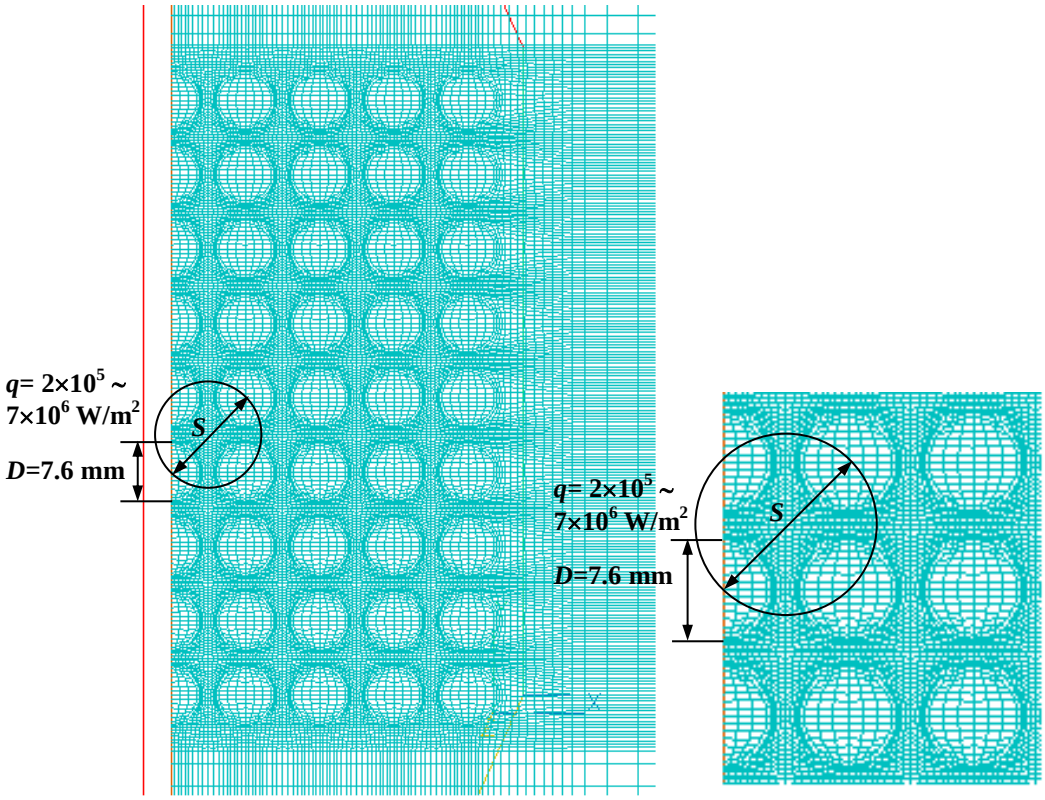

(b) (ESA)

Fig. 3 Boundary fitted coordinates: ESA (a and b).

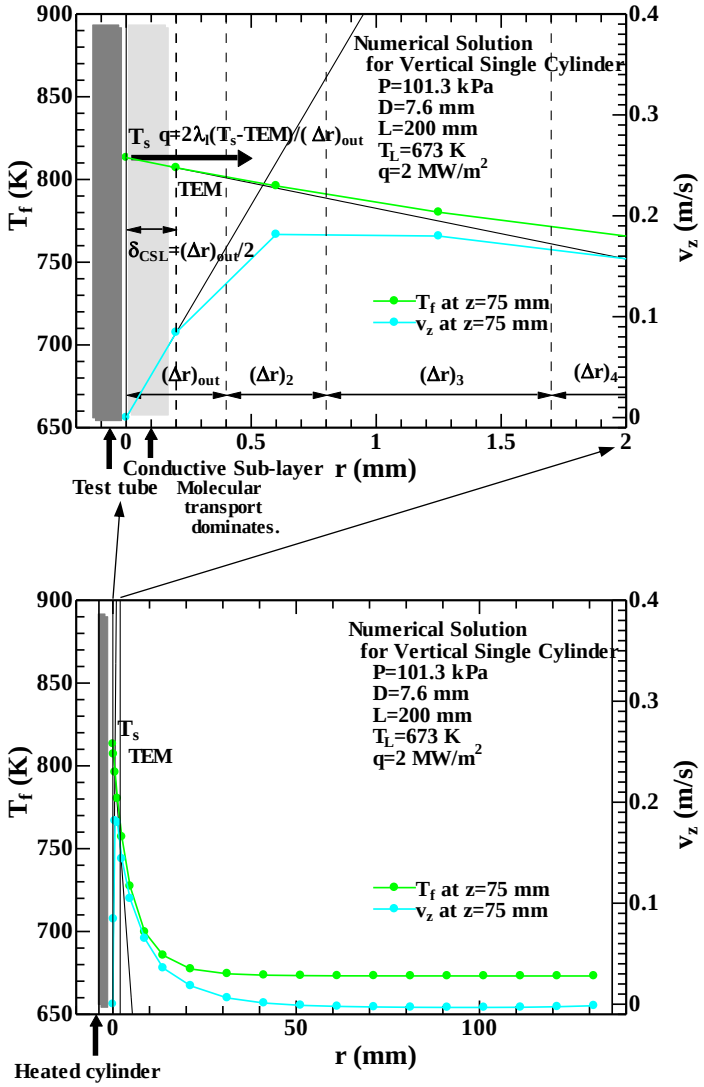

Fig. 4 Liquid temperature of conductive sublayer based on numerically predicted data (solution of unsteady laminar three-dimensional fundamental equation) for a vertical single cylinder with a diameter of 7.6 mm [14-18, 20, 21].

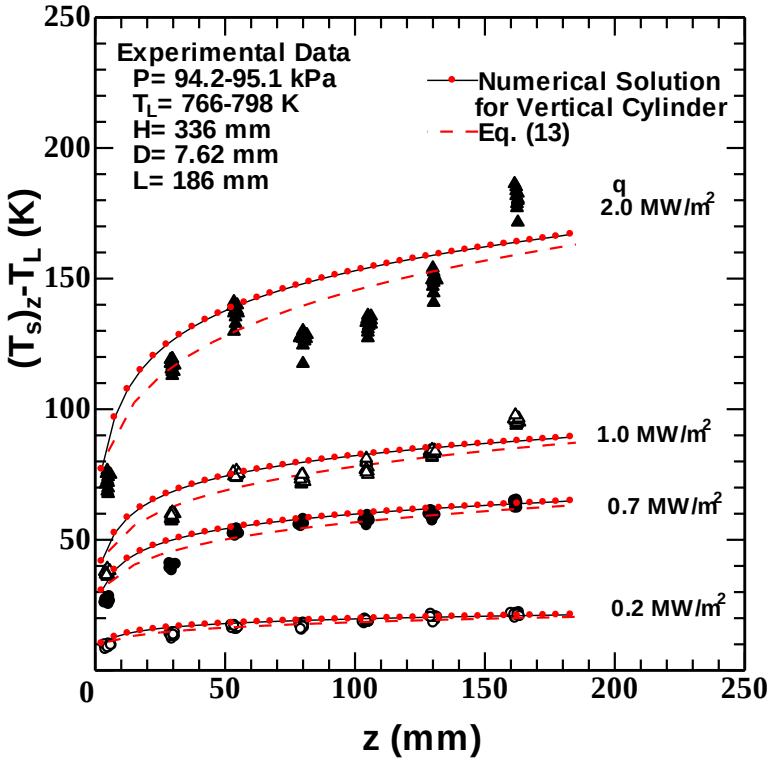

Fig. 5 Experimental data on the local surface temperature rise, $(T_s)_z$-T_L, of a vertical single test cylinder versus the vertical distance from the leading edge of the heated section, z, at heat fluxes of 2×10^5 to 2×10^6 W/m^2 [14] compared with the numerical solutions and Eq. (13).

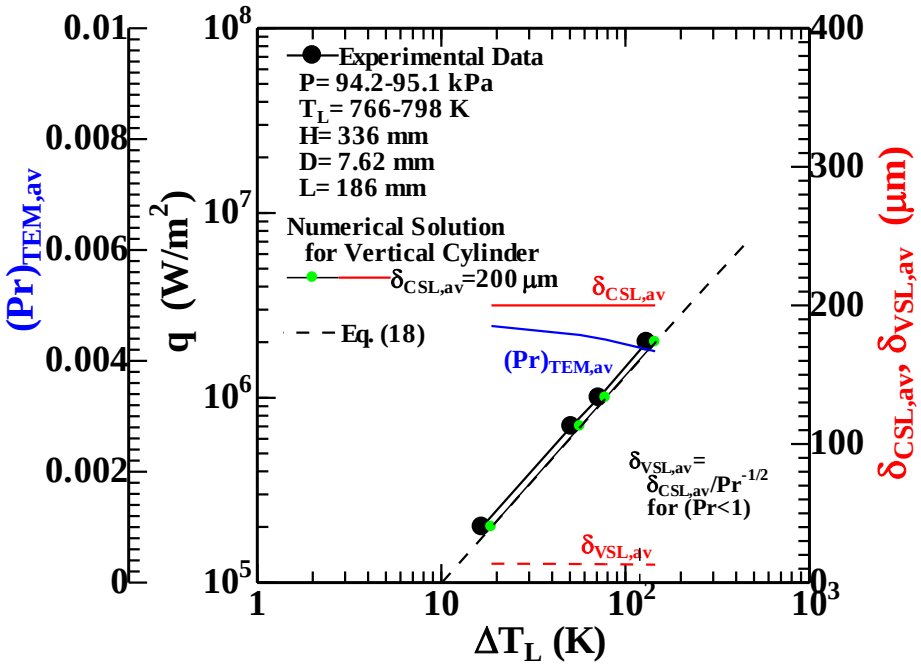

Fig. 6 Heat transfer process (q vs. ΔT_L) on the vertical cylinder, thicknesses of average conductive and viscous sub-layers, and Prandtl numbers evaluated at TEM_{av}, $(Pr)_{TEM,av}$.

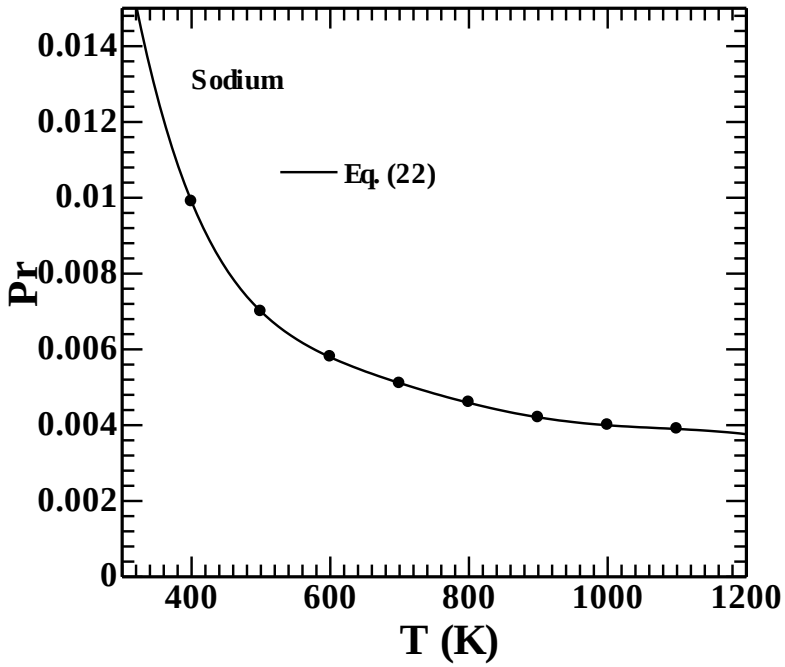

Fig. 7 The relationship between Prandtl number and sodium temperature.

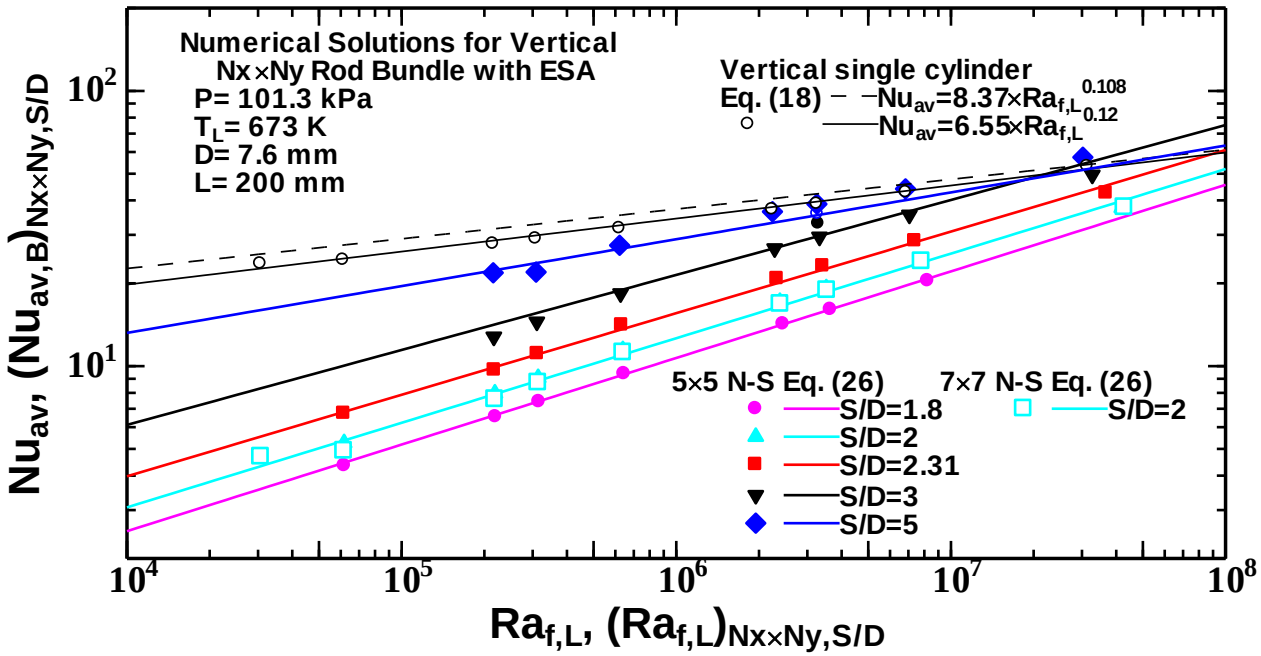

Fig. 8 Theoretical solution, $(Nu_{av,B})_{Nx\times Ny,S/D}$, for vertical 5×5 and 7×7 rod bundles with ESA, Eqs. (26), (27) and (28), and correlation for vertical single cylinder [14-16, 18].

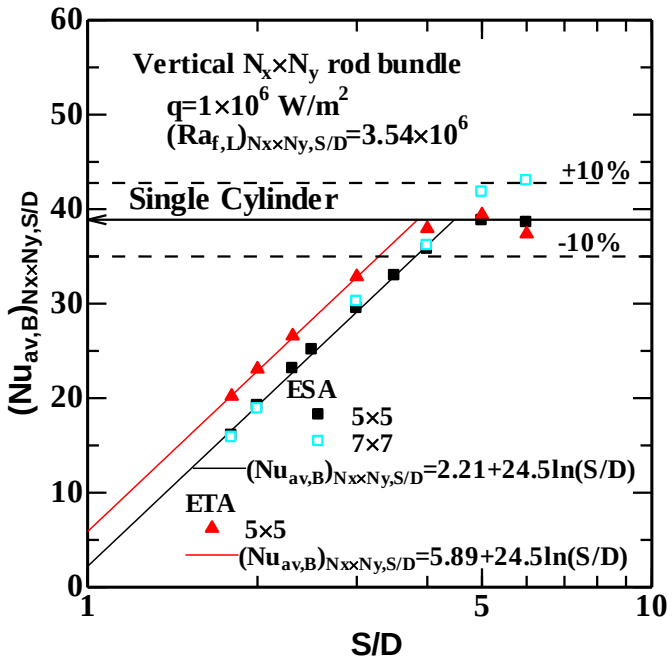

Fig. 9 Average Nusselt number, $(Nu_{av,B})_{Nx\times Ny,S/D}$, for vertical 5×5 and 7×7 rod bundles with ESA and ETA versus the *S/D* at $(Ra_{f,L})_{Nx\times Ny,S/D}=3.54\times10^6$ (q =1×10^6 W/m^2) [14-16, 18].

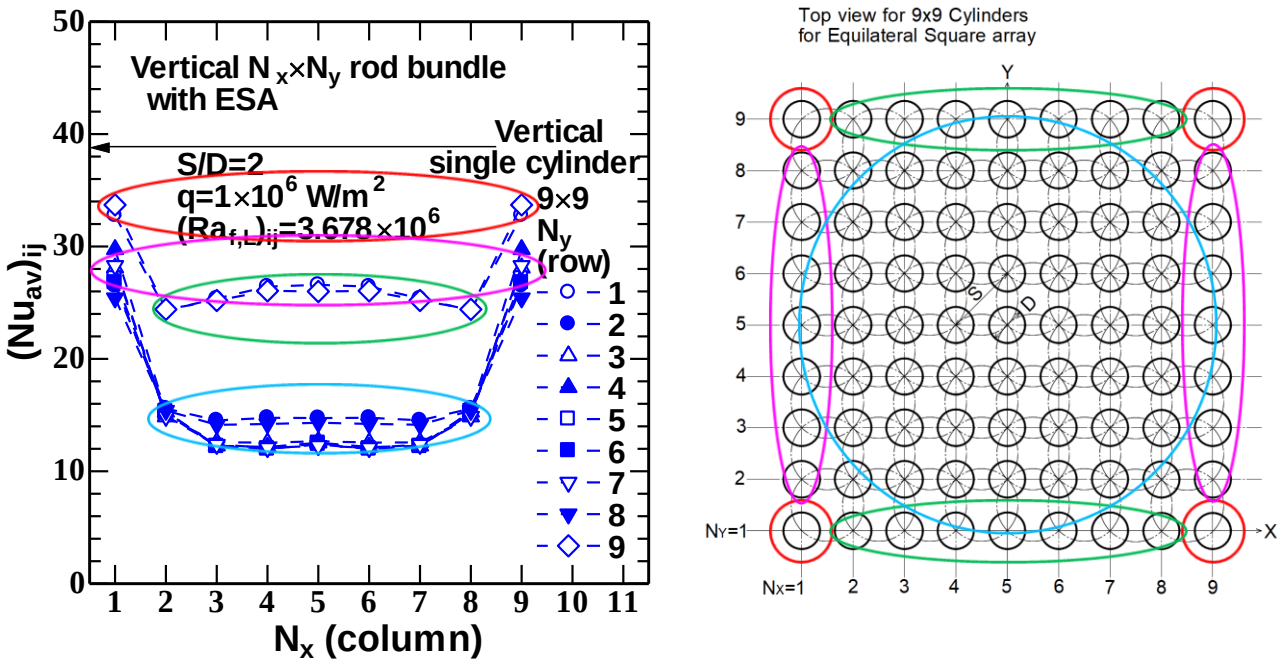

Fig. 10 $(Nu_{av})_{ij}$ versus N_x of a vertical 9×9 rod bundle with ESA with N_y as a parameter at $(Ra_{f,L})_{ij}$= 3.678×10^6 (q = 1×10^6 W/m^2).

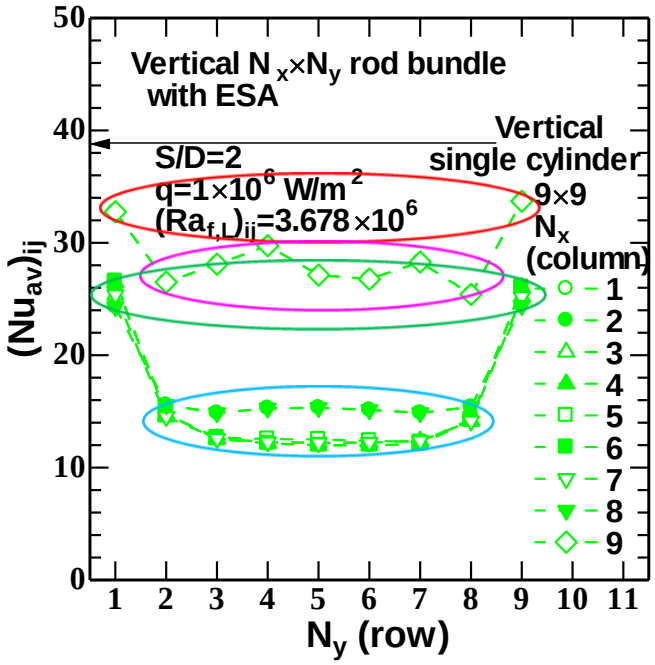

Fig. 11 $(Nu_{av})_{ij}$ versus N_y of a vertical 9×9 rod bundle with ESA with N_x as a parameter at $(Ra_{f,L})_{ij}$= 3.678×10^6 (q = 1×10^6 W/m^2).

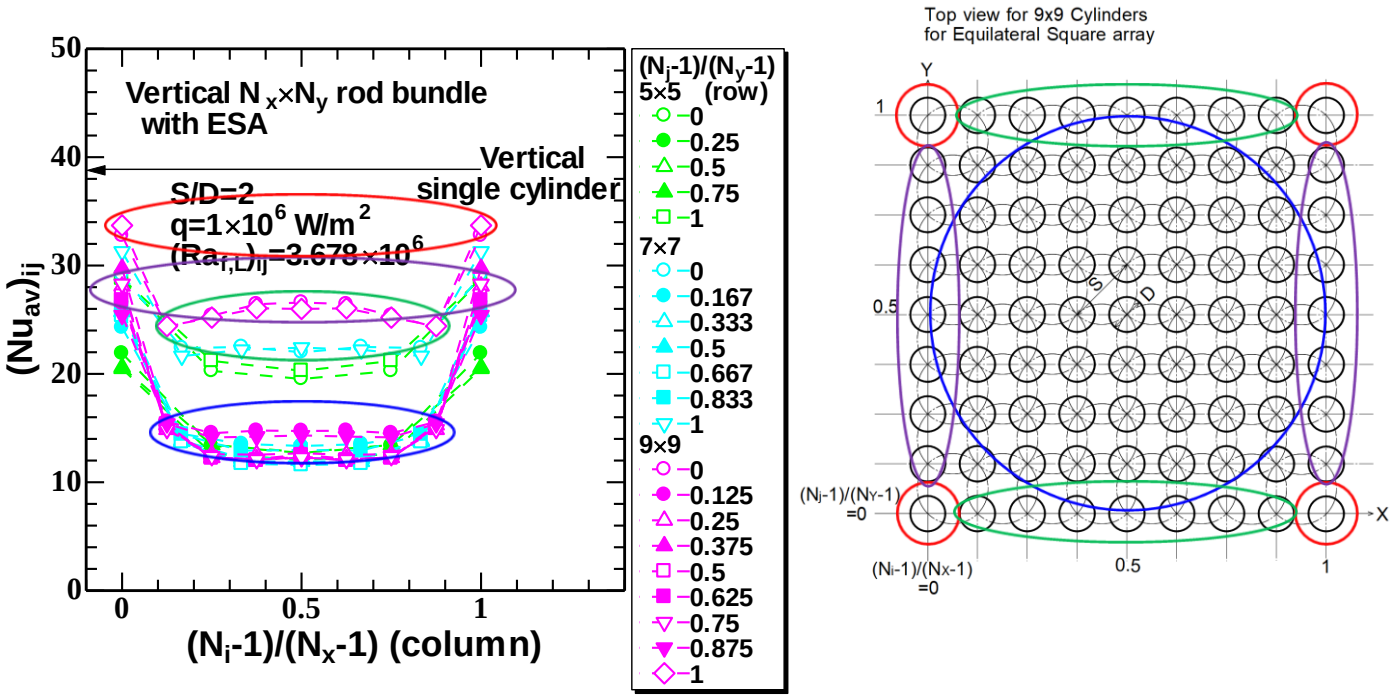

Fig. 12 $(Nu_{av})_{ij}$ versus $(N_i\text{-}1)/(N_x\text{-}1)$ of vertical 5×5, 7×7 and 9×9 rod bundles of ESA with $(N_j\text{-}1)/(N_y\text{-}1)$ as a parameter at $(Ra_{f,L})_{ij}=3.678\times10^6$ ($q = 1\times10^6$ W/m^2) [14-16, 18].

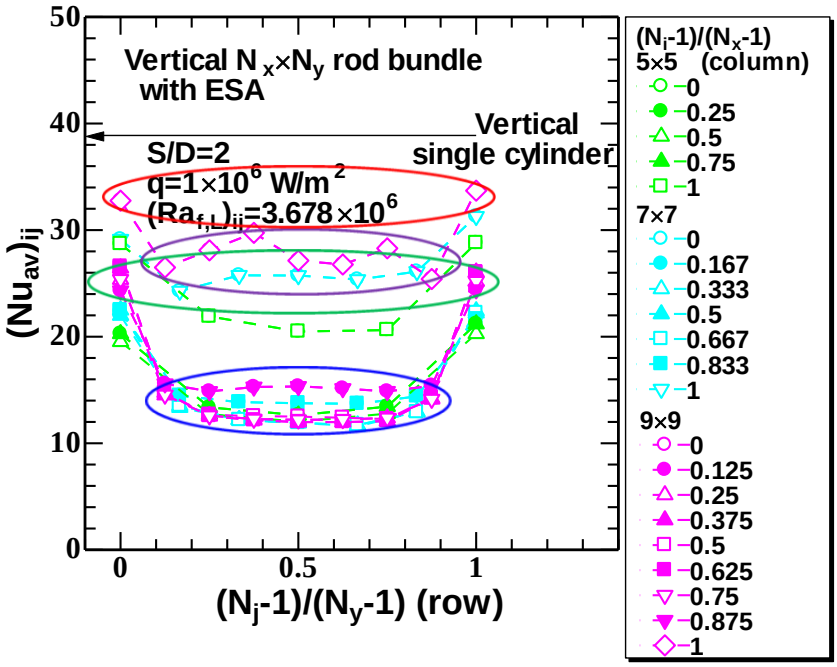

Fig. 13 $(Nu_{av})_{ij}$ versus $(N_j\text{-}1)/(N_y\text{-}1)$ of vertical 5×5, 7×7 and 9×9 rod bundles of ESA with $(N_i\text{-}1)/(N_x\text{-}1)$ as a parameter at $(Ra_{f,L})_{ij}$= 3.678×10^6 (q = 1×10^6 W/m^2) [14-16, 18].

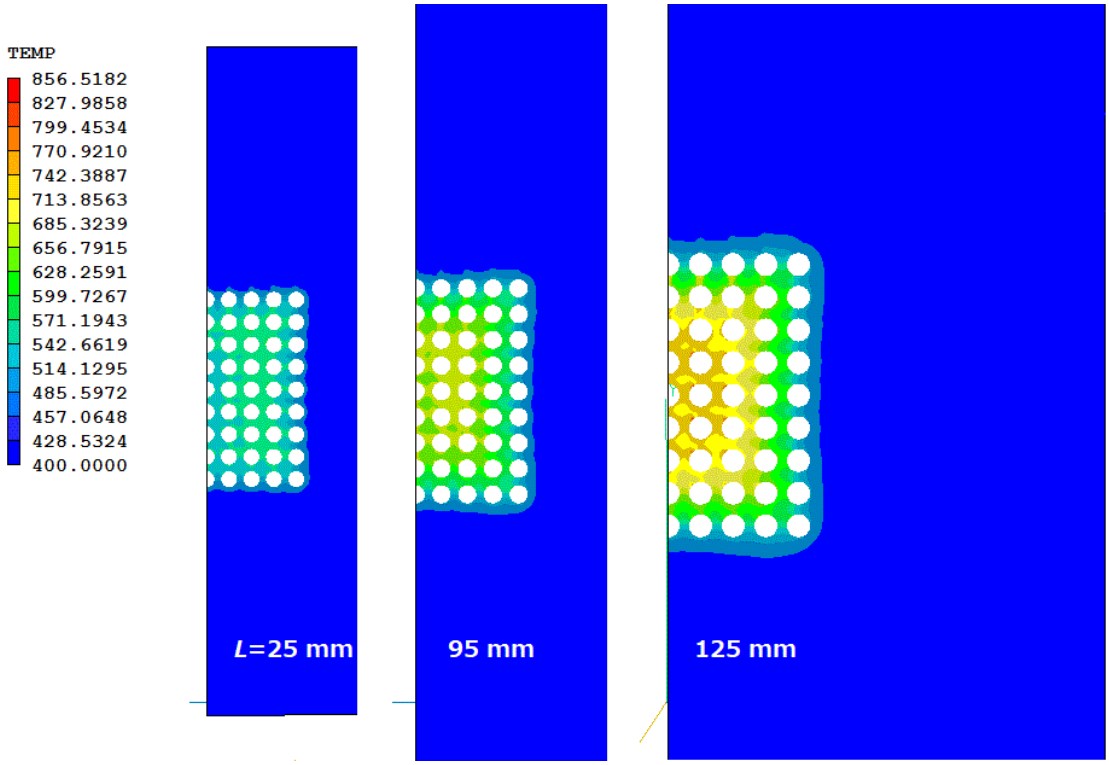

Fig. 14 Liquid temperature contours in the *x*-*y* plane at z = 25, 95, and 195 mm (iz = 11, 18 and 28) for a vertical 9×9 rod bundle of an ESA with S/D = 2 at $(Ra_{f,L})_{9\times9,S/D=2}$= 3.678×10^6 ($q$= 1×10^6 W/m^2).

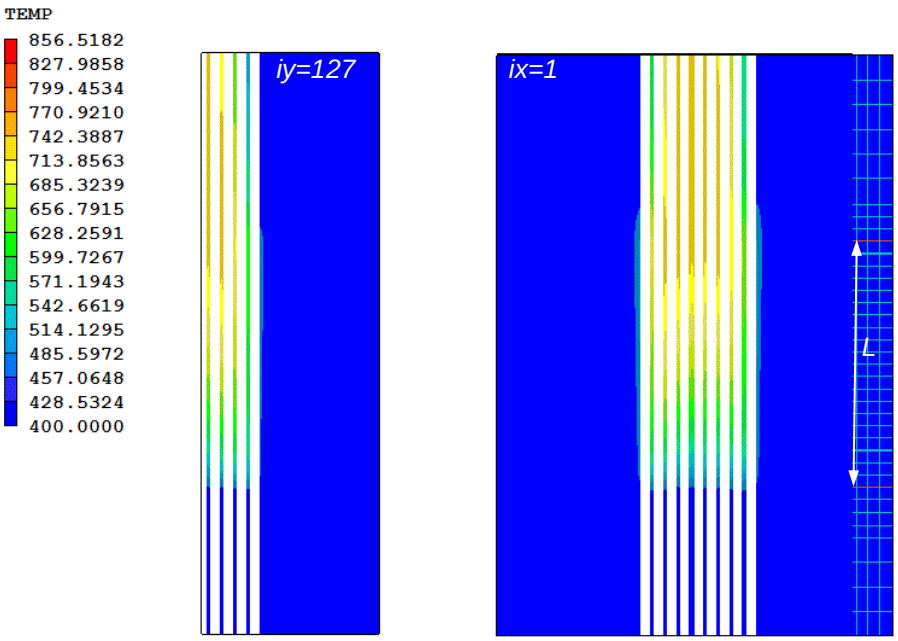

Fig. 15 Liquid temperature contours at the *x*-*z* plane on *iy*=127 and at the *y*-*z* plane on *ix*=1 for vertical 9×9 rod bundle of ESA with *S*/*D* = 2 at $(Ra_{f,L})_{9\times9,S/D=2}$ =3.678×10^6 (q=1×10^6 W/m^2).

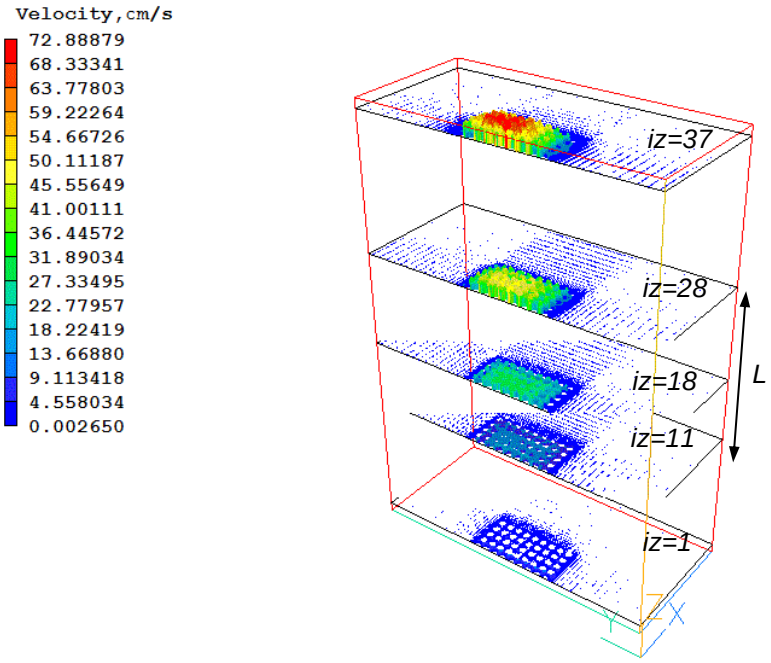

Fig. 16 Distribution of velocity vector of the *x*-*y* plane on *iz*=1, 11, 18, 28 and 37 for vertical 9×9 rod bundle of ESA at *S/D* = 2at $(Ra_{f,L})_{9\times9,S/D=2}$= 3.678×10^6 ($q$=1×10^6 W/m^2).

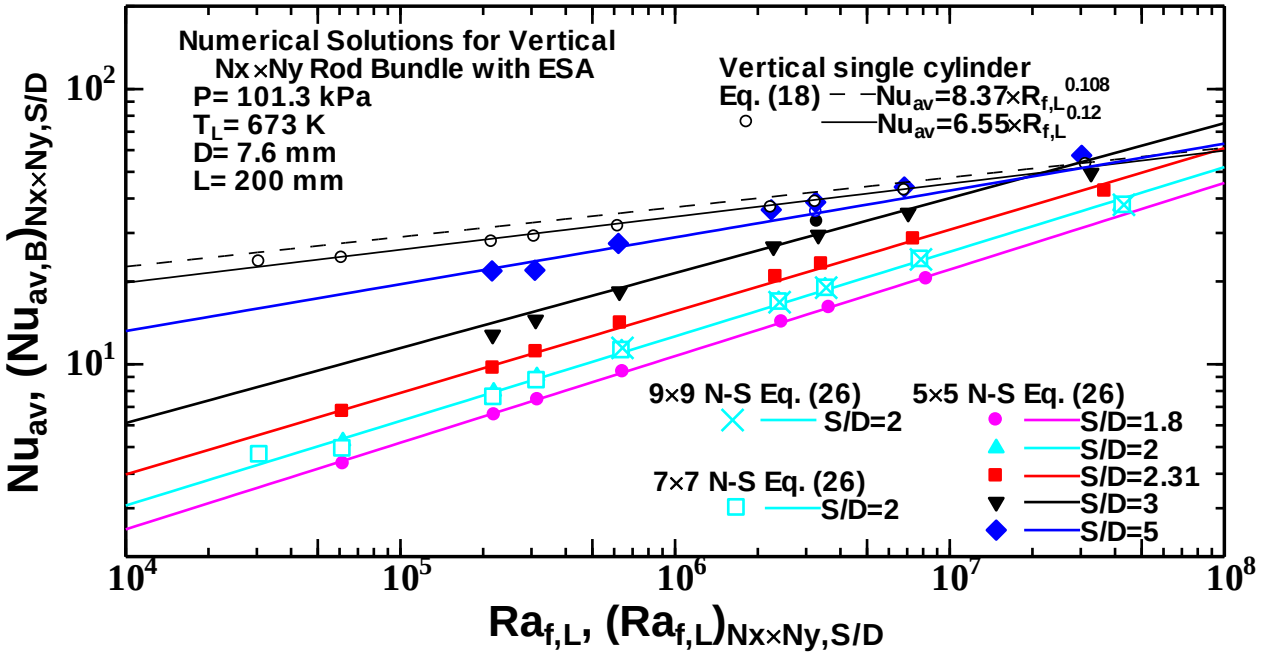

Fig. 17 Theoretical solutions of $(Nu_{av,B})_{9x9,S/D=2}$ for vertical 9×9 rod bundle of ESA with S/D=2, $(Nu_{av,B})_{7x7,S/D=2}$ for vertical 7×7 rod bundle of ESA with S/D=2 [18] and $(Nu_{av,B})_{5x5,S/D}$ for vertical 5×5 rod bundle of ESA with S/D=1.8 to 5 [16], and Nu_{av} for vertical single cylinder [14].

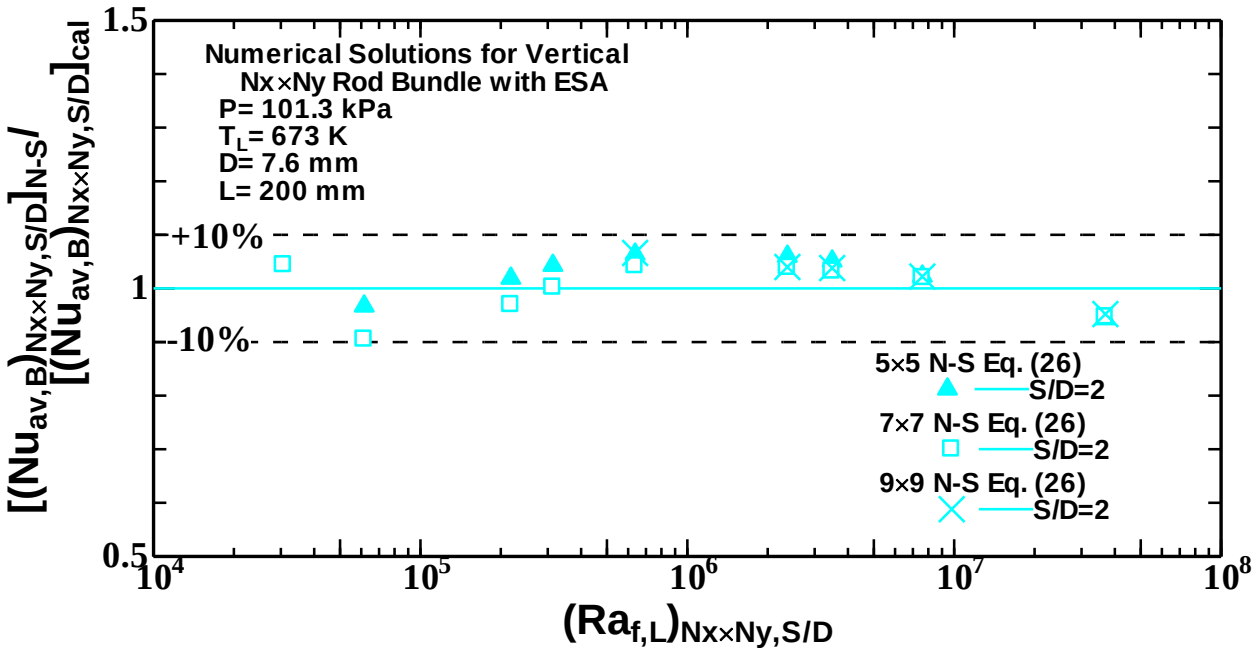

Fig. 18 Comparison of theoretical solutions of $(Nu_{av,B})_{9x9,S/D=2}$ for vertical 9×9 rod bundle of ESA, $(Nu_{av,B})_{7x7,S/D=2}$ for vertical 7×7 rod bundle of ESA [18] and $(Nu_{av,B})_{5x5,S/D=2}$ for vertical 5×5 rod bundle of ESA [16] with authors' correlations, Eqs. (26), (27) and (28).

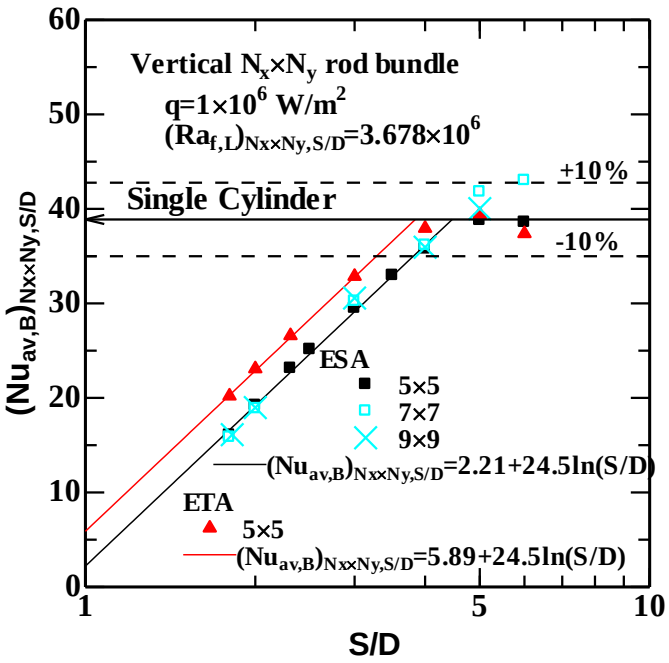

Fig. 19 Average Nusselt number of $(Nu_{av,B})_{Nx\times Ny,S/D}$ for the ESA and ETA versus the S/D at $(Ra_{f,L})_{Nx\times Ny,S/D}=3.678\times10^6$ (q =1×10^6 W/m^2) [16, 18].

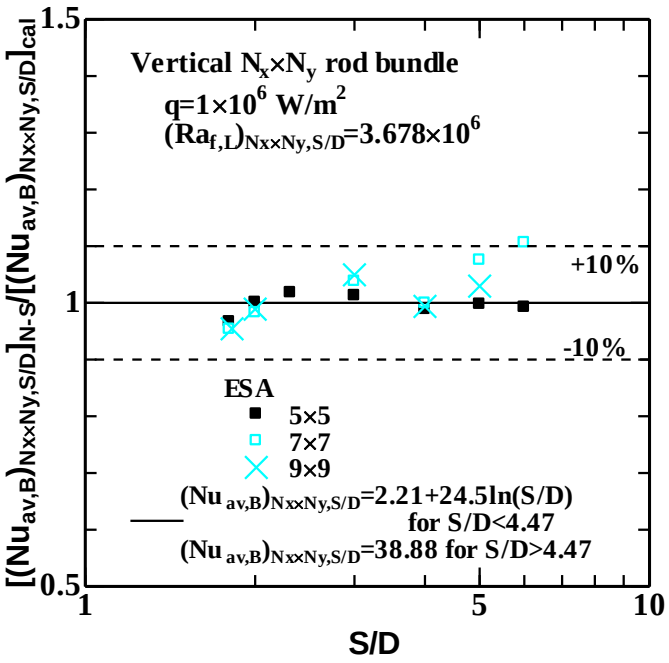

Fig. 20 Comparison of theoretical solutions of $(Nu_{av,B})_{9x9,S/D}$ for vertical 9×9 rod bundle of ESA, $(Nu_{av,B})_{7x7,S/D}$ for vertical 7×7 rod bundle of ESA [18] and $(Nu_{av,B})_{5x5,S/D}$ for vertical 5×5 rod bundle of ESA [16] with authors' correlations, Eqs. (31) and (32).

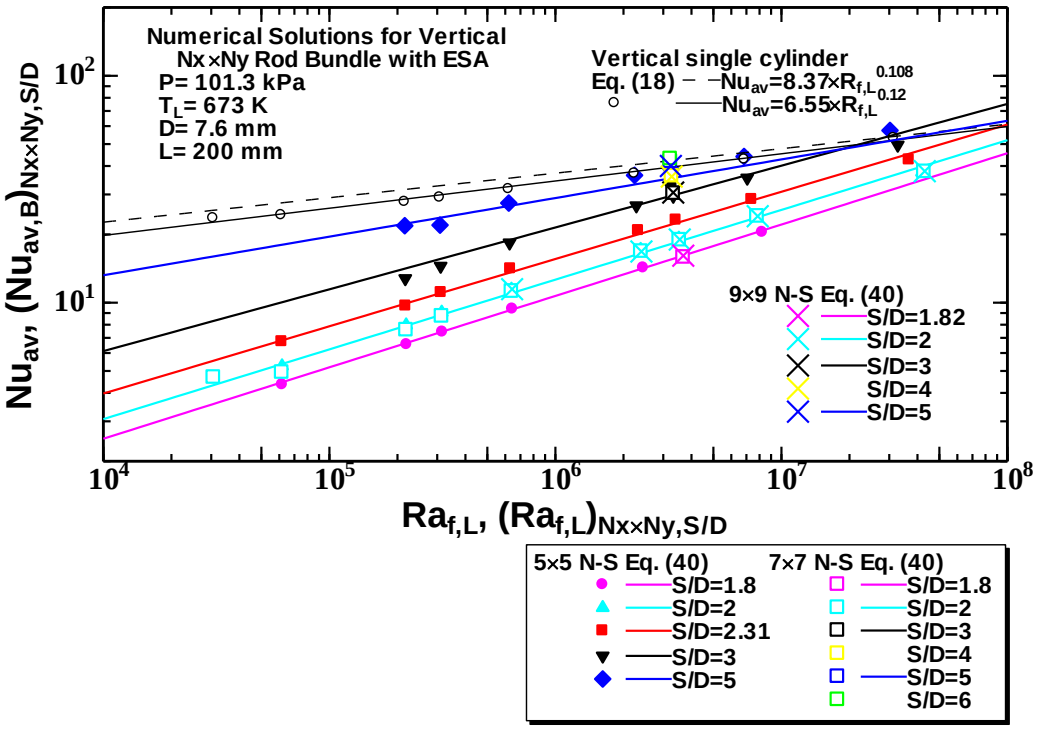

Fig. 21 Theoretical solutions of $(Nu_{av,B})_{Nx\times Ny,S/D}$ for vertical 9×9 rod bundle with ESA from S/D=1.82 to 5, $(Nu_{av,B})_{7x7,S/D}$ for vertical 7×7 rod bundle with ESA from S/D=1.8 to 6 [18], $(Nu_{av,B})_{5x5,S/D}$ for vertical 5×5 rod bundle with ESA from S/D=1.8 to 6 [16], and the Nu_{av} and the correlation for vertical single cylinder [14, 15].

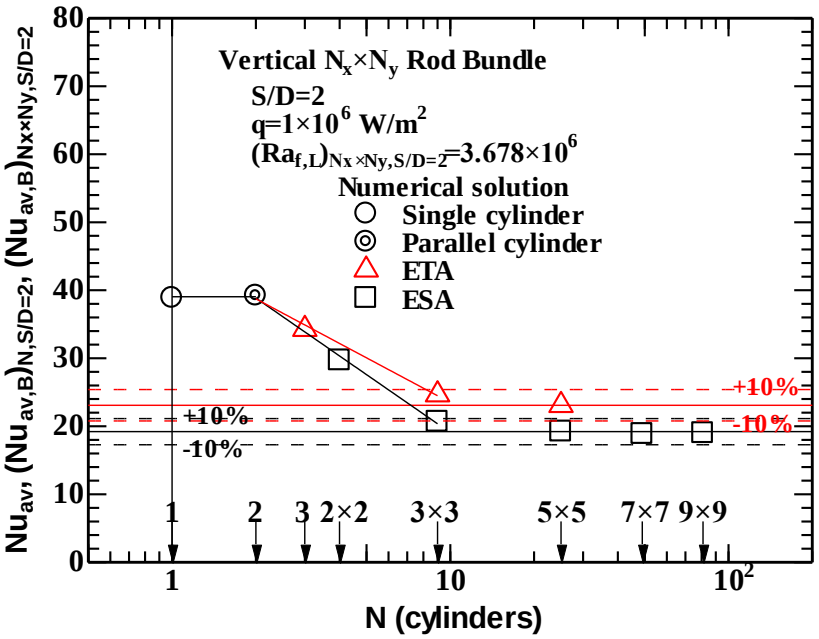

Fig. 22 Average Nusselt number, Nu_{av}, $(Nu_{av,B})_{N,S/D=2}$ and $(Nu_{av,B})_{Nx\times Ny,S/D=2}$, for the ESA and ETA versus the heating element number, N, at $(Ra_{f,L})_{Nx\times Ny,S/D=2}=3.678\times10^6$ (q $=1\times10^6$ W/m^2) [14-16, 18].

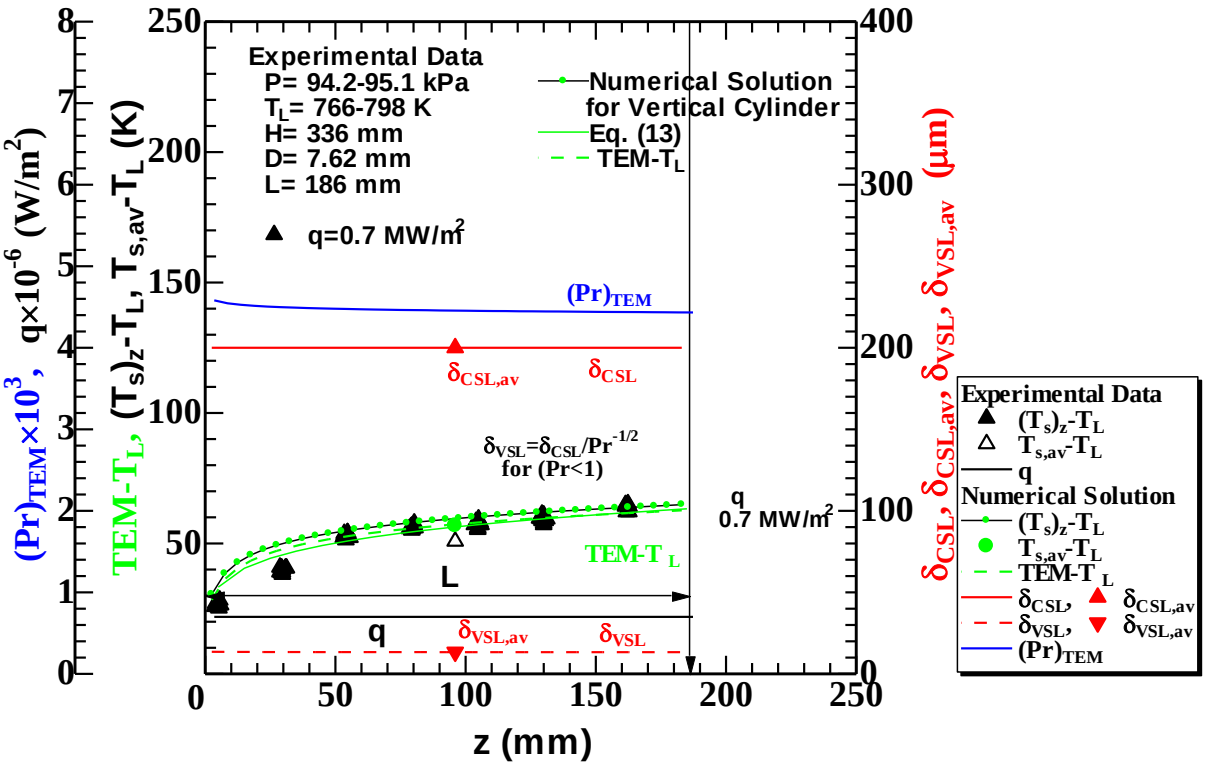

Fig. 23 Local and average surface temperatures at 0.7 MW/m^2 for vertical single test cylinder against the vertical distance from the leading edge of the heated section, *z*, compared with numerical solutions of *TEM-T_L*, local and average surface temperature rises numerically analyzed by δ_{CSL}=200 μm, and δ_{VSL}, $(Pr)_{TEM}$ evaluated at *TEM* on laminar natural convection.

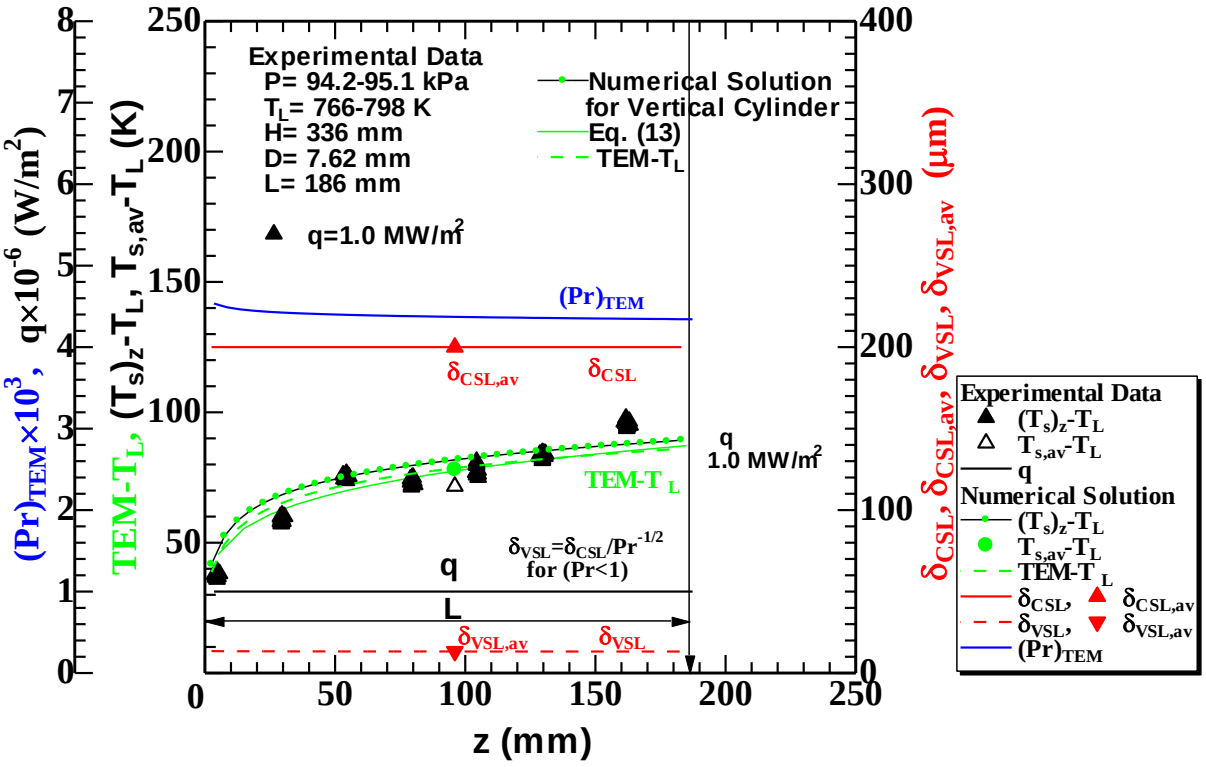

Fig. 24 Local and average surface temperatures at 1.0 MW/m^2 for vertical single test cylinder against the vertical distance from the leading edge of the heated section, *z*, compared with numerical solutions of *TEM-T_L*, local and average surface temperature rises numerically analyzed by δ_{CSL}=200 μm, and δ_{VSL}, $(Pr)_{TEM}$ evaluated at *TEM* on laminar natural convection.

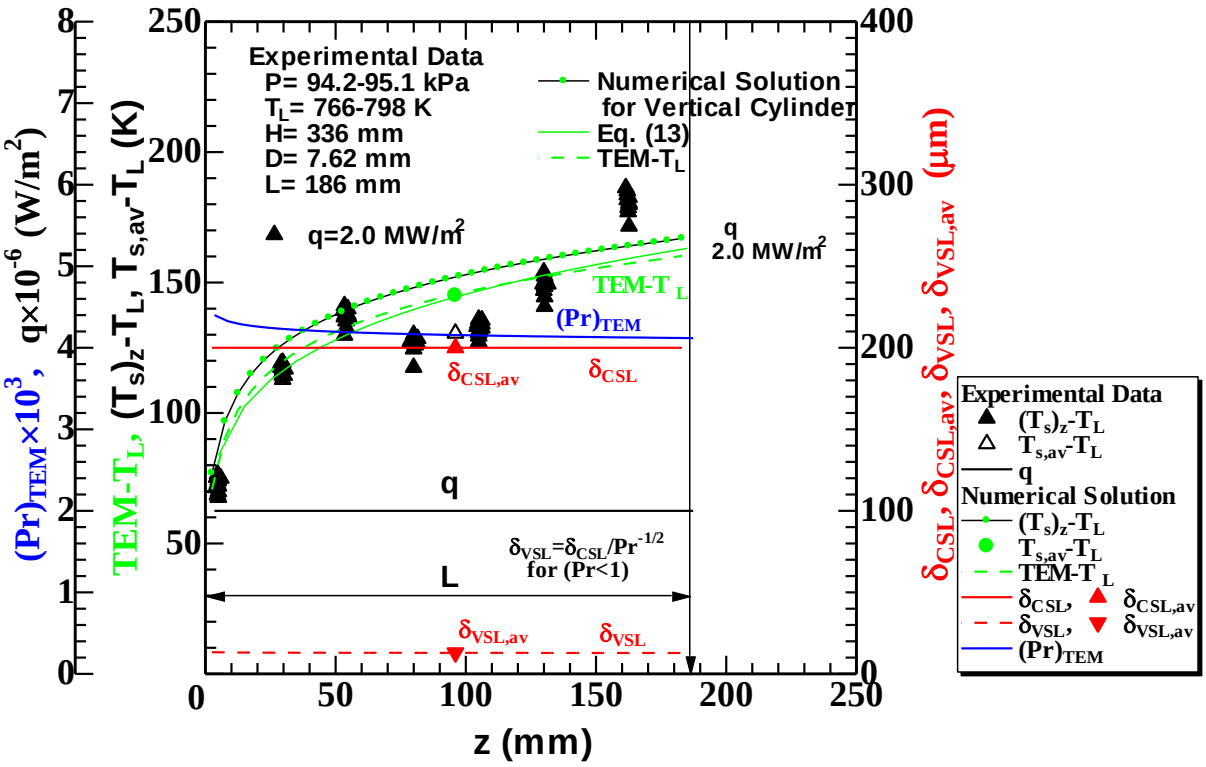

Fig. 25 Local and average surface temperatures at 2.0 MW/m^2 for vertical single test cylinder against the vertical distance from the leading edge of the heated section, *z*, compared with numerical solutions of *TEM-*T_L, local and average surface temperature rises numerically analyzed by δ_{CSL}=200 μm, and δ_{VSL}, $(Pr)_{TEM}$ evaluated at *TEM* on laminar natural convection.